Utilizing a Storm-Generating Hotspot to Study Convective Cloud Transitions: The 1 2 **CACTI Experiment** 3 Adam C. Varble^{1,2}, Stephen W. Nesbitt³, Paola Salio⁴, Joseph C. Hardin¹, Nitin Bharadwaj^{1,5}, 4 Paloma Borque¹, Paul J. DeMott⁶, Zhe Feng¹, Thomas C. J. Hill⁶, James N. Marquis¹, Alyssa 5 Matthews¹, Fan Mei¹, Rusen Öktem^{7,8}, Vagner Castro⁹, Lexie Goldberger¹, Alexis 6 Hunzinger¹, Kevin R. Barry⁶, Sonia M. Kreidenweis⁶, Greg M. McFarquhar¹⁰, Lynn A. 7 McMurdie¹¹, Mikhail Pekour¹, Heath Powers¹², David M. Romps^{7,8}, Celeste Saulo¹³, Beat 8 9 Schmid¹, Jason M. Tomlinson¹, Susan C. van den Heever⁶, Alla Zelenyuk¹, Zhixiao Zhang², and Edward J. Zipser² 10 11 ¹Atmospheric Sciences and Global Change Division, Pacific Northwest National 12 13 Laboratory, Richland, WA ²Department of Atmospheric Sciences, University of Utah, Salt Lake City, UT 14 ³Department of Atmospheric Sciences, University of Illinois at Urbana-Champaign, 15 Urbana, IL 16 ⁴Centro de Investigaciones del Mar y la Atmósfera, Instituto Franco-Argentino para el 17 18 Estudio del Clima y sus Impactos, Universidad de Buenos Aires, Buenos Aires, Argentina ⁵Fortem Technologies, Pleasant Grove, UT 19 ⁶Department of Atmospheric Science, Colorado State University, Fort Collins, CO 20 ⁷Department of Earth and Planetary Science, University of California, Berkeley, CA 21 8 Climate and Ecosystem Sciences Division, Lawrence Berkeley National Laboratory, 22

Early Online Release: This preliminary version has been accepted for publication in *Bulletin of the American Meteorological Society*, may be fully cited, and has been assigned DOI 10.1175/BAMS-D-20-0030.1. The final typeset copyedited article will replace the EOR at the above DOI when it is published.

Berkeley, CA

23

24	⁹ Universidade dos Açores, Ponta Delgada, Portugal
25	¹⁰ Cooperative Institute for Mesoscale Meteorological Studies & School of Meteorology,
26	University of Oklahoma, Norman, OK
27	¹¹ Department of Atmospheric Sciences, University of Washington, Seattle, WA
28	¹² Los Alamos National Laboratory, Los Alamos, NM
29	¹³ Servicio Meteorológico Nacional, Buenos Aires, Argentina
30	
31	Submitted to the Bulletin of the American Meteorological Society
32	9 October 2020
33	
34	Corresponding author: Adam Varble, adam.varble@pnnl.gov
35	

36 ABSTRACT

The Cloud, Aerosol, and Complex Terrain Interactions (CACTI) field campaign was designed to improve understanding of orographic cloud life cycles in relation to surrounding atmospheric thermodynamic, flow, and aerosol conditions. The deployment to the Sierras de Córdoba range in north-central Argentina was chosen because of very frequent cumulus congestus, deep convection initiation, and mesoscale convective organization uniquely observable from a fixed site. The C-band Scanning Atmospheric Radiation Measurement (ARM) Precipitation Radar was deployed for the first time with over 50 ARM Mobile Facility atmospheric state, surface, aerosol, radiation, cloud, and precipitation instruments between October 2018 and April 2019. An intensive observing period (IOP) coincident with the RELAMPAGO field campaign was held between 1 November and 15 December during which 22 flights were performed by the ARM Gulfstream-1 aircraft.

A multitude of atmospheric processes and cloud conditions were observed over the 7-month campaign, including: numerous orographic cumulus and stratocumulus events; new particle formation and growth producing high aerosol concentrations; drizzle formation in fog and shallow liquid clouds; very low aerosol conditions following wet deposition in heavy rainfall; initiation of ice in congestus clouds across a range of temperatures; extreme deep convection reaching 21-km altitudes; and organization of intense, hail-containing supercells and mesoscale convective systems. These comprehensive datasets include many of the first ever collected in this region and provide new opportunities to study orographic cloud evolution and interactions with meteorological conditions, aerosols, surface conditions, and radiation in mountainous terrain.

59 CAPSULE

63

60	The CACTI field campaign provides comprehensive atmospheric state, aerosol, cloud,
61	precipitation, surface, and radiation measurements to improve understanding of convective
62	cloud life cycle interactions with their surrounding environment.

1. Introduction

64

65

66

67

68

69

70

71

72

73

74

75

76

77

78

79

80

81

82

83

84

85

86

87

The U.S. Department of Energy (DOE) Atmospheric Radiation Measurements (ARM) Cloud, Aerosol, and Complex Terrain Interactions (CACTI) field campaign was recently completed over a 7-month period from October 2018 through April 2019 in the Sierras de Córdoba (SDC) range of central Argentina. A primary goal was to use the high frequency of orographically initiated convective clouds to comprehensively study the complex interactions between meteorology, aerosols, complex terrain, and convective cloud life cycles. This article summarizes the campaign while highlighting ongoing and potential future research using its unique datasets. Complex terrain provides a natural laboratory to study a range of cloud types and processes because of how frequently clouds anchor to specific topographic features. These features often strongly impact atmospheric circulations that commonly affect cloud and thunderstorm formation (Houze 2012). Many mountainous regions of the world exert a primary control on the initiation of deep convection that often grows upscale into mesoscale convective systems (MCSs), producing a majority of rainfall downstream of these regions (e.g., Laing and Fritsch 1997; Nesbitt et al. 2006; Durkee et al. 2009). Poor prediction of deep convection initiation timing and location (e.g., Dai 2006), upscale growth from isolated to mesoscale systems (e.g., Hohenegger and Stevens 2013; Hagos et al. 2014), propagation (e.g., Del Genio et al. 2012; Song et al. 2013), and surface flux-precipitation interactions (e.g., Taylor et al. 2012; Klein and Taylor 2020; Qian et al. 2020) likely contribute to a warm, dry bias in climate models downstream of the SDC range (Carril et al. 2012; Solman et al. 2013) and other mountain ranges such as the Rockies (Anderson et al. 2003; Klein et al. 2006), which are key agricultural regions. Increasing model resolution has improved predictions, but even models without parameterized deep convection tend to display overly

strong updrafts (Varble et al. 2014a, Marinescu et al 2016; Fan et al. 2017), excessive riming that results in high-biased radar reflectivity (e.g., Lang et al. 2011; Varble et al. 2011; Fridlind et al. 2012; Stanford et al. 2017), and low-biased stratiform rainfall (e.g., Hagos et al. 2014; Varble et al. 2014b, Han et al. 2019). Improving the representation of these systems as a function of environmental conditions in multi-scale models will help to answer the question of how water and food resources will change in a changing climate. Recent experiments including CuPIDO (Damiani et al. 2008), COPS (Wulfmeyer et al. 2008), and DOMEX (Smith et al. 2012), have sought to better understand orographic cumulus and deep convective cloud life cycles. While these and many other non-orographic campaigns have contributed substantially to our understanding of interactions between clouds and their surrounding environment, sampling limitations have left open critical questions.

The wide range of environmental conditions in central Argentina and the high frequency of orographic convective clouds that evolve into deeper congestus, initiate into deep convection (Rasmussen and Houze 2011, 2016; Mulholland et al. 2018), and organize into mesoscale systems near the SDC range (Anabor et al. 2008; Romatschke and Houze 2010; Rasmussen et al. 2014, 2016) make it an ideal location to quantify interactions between convective clouds and their surrounding environment. Extreme storms in Argentina stand out as being some of the world's deepest (Zipser et al. 2006), largest (Velasco and Fritsch 1987), and longest-lived (Durkee and Mote 2009) with some of the highest lightning flash rates (Cecil et al. 2015) and largest hail (Cecil and Blankenship 2012; Kumjian et al. 2020) on Earth. The convective lifecycle in this region is significantly influenced by orographic flows (Nicolini and Skabar 2011; Rasmussen and Houze 2011; Bueno Repinaldo et al. 2015; Mulholland et al. 2019, 2020), the South American low level jet (Nicolini et al. 2002; Salio et al. 2002, 2007; Saulo et al. 2004, 2007; Borque et al. 2010), and synoptic-scale troughs that induce the Northwestern Argentinean ("Chaco") Low (Seluchi et al. 2003), free tropospheric subsidence (Ribeiro and

Bosart 2018), eastward propagating drylines (Bechis et al. 2020), and northward propagating cold fronts (Seluchi et al. 2006) east of the Andes. Changes in land surface properties throughout the October-April warm season during which most precipitation falls impact surface fluxes and boundary layer evolution on daily and seasonal time scales that feed back to cloud and rainfall generation (e.g., Saulo et al. 2010; Sörensson and Menéndez 2011; Ruscica et al. 2015). Finally, local and long-range transport of biomass burning smoke (Freitas et al. 2005; Camponogara et al. 2014, Della Ceca et al. 2018) and blowing dust impact aerosol properties in the region (Winker et al. 2013), but much remains unknown because of limited measurements in the region.

2. Objectives

- The unique atmospheric conditions of central Argentina coupled with the motivation to better understand two-way interactions between convective clouds and their surrounding environment motivated the CACTI field campaign. The experiment was designed to address the following primary science questions:
- 1. How do orographically-generated cumulus humilis, mediocris, and congestus 129 clouds interact with and depend on environmental flows, thermodynamics, aerosols, and 130 surface properties?
 - 2. What combinations of environmental conditions promote or suppress deep convection initiation, upscale growth, and mesoscale organization, and how do deep convective systems alter surface and aerosol properties?
 - This multifaceted experiment involved deployment or an ARM mobile facility (AMF1; Mather and Voyles 2013) and the C-band Scanning ARM Precipitation Radar (C-SAPR2) for a long term 6.5-month Extended Observing Period (15 October 2018 30 April 2019), and a

1.5-month Intensive Observation Period (IOP, 1 November – 15 December 2018) that included Gulfstream-1 (G-1) aircraft flights. The campaign overlapped with the collaborating multiagency, National Science Foundation (NSF) led Remote sensing of Electrification, Lightning, And Mesoscale/microscale Processes with Adaptive Ground Observations (RELAMPAGO) field campaign (see companion article by Nesbitt et al. 2020).

The processes targeted by CACTI measurements are shown in Figure 1. One goal was to measure impacts of boundary layer evolution, orographic thermal and mechanical flows, occasional northerly low-level jets, and free tropospheric conditions on the evolution of orographic cumulus, stratocumulus, and deeper convective clouds. North-south oriented orographic cumulus cloud lines formed most frequently to the west of the AMF1 site over or just east of the highest terrain, fed by air east of the SDC when clouds were coupled with the boundary layer. Free tropospheric flow typically had a westerly component, causing congestus clouds to shear toward the AMF1. In these situations, a primary goal was to measure the cloud base inflow aerosol and thermodynamic properties while retrieving evolving properties of clouds and detrained air aloft through remote sensing, radiosondes, and the G-1. A second goal was to measure processes associated with the formation of rain and ice in convective clouds that led to deep convection initiation, in addition to processes that promoted or suppressed deep convective upscale growth into mesoscale complexes, for example through cold pool outflow interactions with the complex terrain and ambient atmospheric conditions. A third goal involved measurement of the impacts of clouds and precipitation on free tropospheric thermodynamics, aerosol wet deposition, and surface moistening, and how these impacts affected subsequent clouds.

159

160

137

138

139

140

141

142

143

144

145

146

147

148

149

150

151

152

153

154

155

156

157

158

3. Observational Strategy

a. Ground Deployment

161

162

163

164

165

166

167

168

169

170

171

172

173

174

175

176

177

178

179

180

181

182

183

184

185

The AMF1 with over 50 instruments was deployed with the C-SAPR2 to a rural location at 1141 m elevation just east of Villa Yacanto, Argentina. The location was on the eastern slopes of the SDC, about 20 km from the primary north-south oriented ridgeline crest that rises 2000 m above the surrounding plains (Figure 2). Radar beam blockage was minimal apart from the lowest levels to the west where the higher terrain was located. The AMF1 was also well offset from anthropogenic aerosol sources to the northeast where the prevailing flow originated. Views of the site are shown in Figure 3. Additional sites included a second sounding and meteorological station at Villa Dolores Airport west of the mountains, two high-elevation meteorological stations between the AMF1 and Villa Dolores sites, and camera sites offset 1-2 km from the AMF1 for stereo photogrammetry. Figure 2 also shows operational Córdoba sounding and radar sites, and fixed RELAMPAGO sites where C-band radars and a differential absorption lidar were deployed for a portion of CACTI. The extensive ground instrumentation deployed for CACTI and their primary measurements are shown in Table 1. Although the campaign officially began October 15, most measurements began in late September. Scanning Ka-, X-, and C-band radars and a vertically pointing Ka-band radar made critical cloud and precipitation measurements. The radar scan strategy targeted the evolution of close by convective clouds. The C-SAPR2 performed a 15tilt plan position indicator (PPI) "volume" between elevation angles of 0.5° and 33° followed by a vertically pointing, azimuthally rotating ("bird bath") ZPPI, and two 6-azimuth hemispheric range-height indicator (HSRHI) patterns along the radials shown in Figure 2. Hemispheric (HS) in this context refers to scanning from one horizon to the other (180° in elevation) at a constant azimuth. This sequence was repeated every 15 minutes. The X/Ka-SACR also performed a 15-minute sequence with a 30°-wide sector RHI scan between west-

southwest and west, followed by the HSRHI pattern repeated three times. The sector RHI was

performed because 4 HSRHI patterns could not be comfortably fit into a 15-minute sequence, but it also provides a limited volume with high vertical resolution within the field of view of stereo cameras from which cloud boundary retrievals are possible.

Periods of C-SAPR2 pedestal mechanical issues began in late December, and by early March, the azimuthal motor failed. At this time, the C-SAPR2 was reconfigured to perform a west-east HSRHI pattern with 45-second updates for the rest of the campaign. The X/Ka-SACR then began performing PPI volumes, replacing the sector RHI and one of the HSRHI patterns in each 15-minute sequence. These volumes had a shorter range (60 km vs. 110 km), lower angular resolution, and greater attenuation in heavy precipitation than C-SAPR2 volumes but filled the PPI volume gap for the rest of the campaign.

Additional cloud and precipitation measurements were continuously made by disdrometers, rain gauges, cameras, microwave radiometers, lidars and a total sky imager. Radiosondes were the most critical instrument for measuring atmospheric state. At the AMF1 site, they were launched every 3-4 hours between 9 AM and 9 PM local (12 and 00 UTC). The sounding site at Villa Dolores launched at 9 AM and 3 PM (12 and 18 UTC). Additional atmospheric kinematic and thermodynamic information was provided by surface meteorological stations, microwave radiometers, an Atmospheric Emitted Radiation Interferometer, a Doppler lidar, a radar wind profiler, and a sodar. Surface conditions were monitored with eddy correlation flux measurement and surface energy balance systems. Exhaustive spectral and broadband, upwelling and downwelling, shortwave and longwave radiation measurements were made by a number of radiometers. Lastly, comprehensive aerosol scattering, absorption, size distribution, and chemical composition measurements were made along with concentrations of condensation nuclei, cloud condensation nuclei at several supersaturations, ice nucleating particles, and several trace gases.

211 b. Aircraft Deployment

212

213

214

215

216

217

218

219

220

221

222

223

224

225

226

227

228

229

230

231

232

233

234

The G-1 (Schmid et al. 2014) completed 22 flights between November 4 and December 8 totaling 79.4 hours of flight time (Figure 4). The instrumentation payload and measurements made are shown in Table 2, and each flight is described in Table 3. Nineteen flights sampled cumulus humulis, cumulus congestus, or stratocumulus clouds with most having clear ties to the topography, while 8 included initiation of deep convection during or shortly after flights. Flight summaries can be downloaded on the RELAMPAGO field catalog available through the National Center for Atmospheric Research Earth Observing Laboratory (NCAR EOL; catalog.eol.ucar.edu/relampago). Aircraft position and atmospheric state measurements with 1-100 Hz sampling were made by a number of instruments. Comprehensive aerosol measurements overlapped significantly with measurements made continuously at the surface AMF1 site and included aerosol scattering and absorption, size distribution, and chemical composition in addition to condensation nuclei, cloud condensation nuclei, ice nucleating particle, and trace gas concentrations. In situ cloud properties measured included bulk condensed water content from several sensors, a cloud particle imager, and hydrometeor size distributions. Most flights performed north-south, constant-altitude legs over the AMF site, over the highest terrain where clouds were most frequent, and to the west of the clouds and highest terrain (Figure 4). Legs were flown just below cloud base (when possible), at mid cloud level through cloud and to its west and east, and at cloud top, repeating in time. Some flights also included a spiral down over the AMF site to provide an aerosol and thermodynamic profile. Deviations from this strategy were performed on occasion based on meteorological or cloud conditions. The aerosol isokinetic inlet was used to sample the clear sky aerosol population above, below, and adjacent to clouds. The counterflow virtual impactor (CVI) inlet was used

for in-cloud sampling, to characterize cloud droplet residuals, and compare their sizes and compositions to particles outside clouds.

c. Coordination with the RELAMPAGO Field Campaign

CACTI coincided with the RELAMPAGO field campaign (see companion article by Nesbitt et al. 2020) which included a hydrologic component from June 2018 through April 2019 and an IOP between November 2018 and January 2019. RELAMPAGO and CACTI teams coordinated operations due to their shared goals of targeting initiating and growing deep convective clouds. The CACTI PI and some science team members were commonly located with the RELAMPAGO science team at the RELAMPAGO operations center in Villa Carlos Paz. Forecasts and near real time data displays utilized for RELAMPAGO mobile missions were also utilized for the adaptive observing components of CACTI during the IOP. During RELAMPAGO mobile missions, the CACTI observing sites were commonly used as part of the RELAMPAGO observing network.

The integration of these two campaigns has resulted in synergistic usage of data from RELAMPAGO and CACTI instrumentation for a number of studies. For example, RELAMPAGO radar measurements are being used with C-SAPR2 for multi-Doppler retrieved boundary layer and cloud dynamics during initiating and growing deep convection (Marquis et al. 2021) within the dense RELAMPAGO radiosonde networks during mobile missions. These well-sampled, better characterized RELAMPAGO IOP cases will contextualize the many additional cases observed during CACTI, while CACTI radar rain rate retrievals will help contextualize the long-term RELAMPAGO hydrologic observations.

4. Operations and Outreach

258

259

260

261

262

263

264

265

266

267

268

269

270

271

272

273

274

275

276

277

278

279

280

281

Most CACTI instruments operated continuously and were monitored by ARM site technicians and engineers; however, some measurements were adjusted in response to weather forecasts or real-time observations. During the IOP, forecasts were provided by members of Servicio Meteorológico Nacional (SMN) and graduate students. Forecasts typically used global numerical weather prediction and regional convection-allowing model guidance that was run every 6-12 hours by SMN, the University of Illinois, and Colorado State University (CSU). When deep convection was forecasted, AMF1 radiosonde launch frequency was increased from 4-hourly to 3-hourly between 9 AM and 9 PM local. Additional sondes were also occasionally launched from the Villa Dolores site. In addition, Geostationary Operational Environmental Satellite (GOES-16) mesoscale domain sectors (MDSs) with 1-min updates were requested from the National Oceanic and Atmospheric Administration (NOAA) on these days with most requests granted. This data is available from the NOAA Comprehensive Large Array-Data Stewardship System (CLASS; www.class.noaa.gov). Outside of the IOP, model forecast guidance was used to coordinate daily radiosonde launch schedules and MDS requests. In addition, during select IOP daytime periods, the C-SAPR2 HSRHI radar scans were modified on site to target specific convective cells with sector RHIs. Forecasts also informed flight planning for the next day, which consisted of a pattern and takeoff time that were decided upon by the PI, G-1 manager, and lead pilot on site in Río Cuarto. Updated forecasts and real time conditions were checked at least 4 hours prior to takeoff to determine whether the flight takeoff should be delayed based on unexpected conditions. While airborne, G-1 flights were monitored in real time with radar, satellite, lightning, and flight track displays at the RELAMPAGO operations center. The lead flight scientist would communicate with the PI to adjust flight legs and updates were sent if inclement weather approached the flight operating area. Debriefs followed each flight, and mission summaries were written and uploaded to the RELAMPAGO field catalog.

Outreach efforts were performed by team members and ARM staff, facilitated by Investigación Aplicada (INVAP S.E.), who helped to manage CACTI. Prior to the start of CACTI, Paola Salio performed local outreach to explain instrumentation that would be installed just outside of Villa Yacanto. A day-long outreach event was then held at the AMF1 site at the start of the IOP. Members of the public and media were invited along with local high school students to learn about site instrumentation, measurements, operations, and scientific objectives including why the site was chosen and how the science that it would facilitate would benefit future weather and climate prediction in the region. A second outreach event was held at the Río Cuarto Airport where the G-1 was located. Members of the public, students, the media, airport officials, and governmental officials toured the aircraft and learned about the aircraft measurements and operations component of CACTI. Throughout the campaign, smaller groups of students, scientists, and members of the media were also able to visit the AMF1 site.

5. Data Processing and Retrievals

Data collected during CACTI are available through over 200 datastreams within the ARM archive searchable through the DOE ARM CACTI website (www.arm.gov/research/campaigns/amf2018cacti). Over 20 ARM value added products that combine several datastreams into geophysical retrievals have been completed or are in progress. With ARM VAP names in parentheses, they include quality controlled radiative flux measurements (RADFLUXANAL), aerosol optical properties (AOP), and corrected surface fluxes (QCECOR). Environmental thermodynamic and kinematic products include planetary

boundary layer height estimates from soundings (PBLHT), microwave radiometer retrieved precipitable water (MWRRET), Doppler lidar retrieved horizontal and vertical winds (DLPROF), AERI-estimated lower tropospheric temperature and humidity (AERIOE), interpolated soundings (INTERPSONDE), and variational analysis retrieved large-scale forcing (VARANAL). Cloud products include cloud optical depth (MFRSRCLDOD), combined lidar-radar time-height cloud boundaries (KAZRARSCL), microwave radiometer retrieved liquid water path (MWRRET), radar variables derived from disdrometers (LDQUANTS, VDISQUANTS), Cartesian gridded multi-frequency scanning radar RHIs (KASACRGRIDRHI, XSACRGRIDRHI), and multi-scale GOES-16 cloud retrievals provided by the National Aeronautics and Space Administration (VISST). All radar data collected were calibrated following Hardin et al. (2020) and Hunzinger et al. (2020) using changes in ground clutter signals as a measure of drift relative to absolute calibration measured via corner reflector at a single time.

In addition to data provided by ARM, additional PI products have been or will soon be completed. Aerosol products include ice-nucleating particle (INP) concentrations and composition as a function of temperature processed at CSU from collected surface and aircraft samples, and single particle size and chemical composition aboard the aircraft from the miniSPLAT (Zelenyuk et al. 2010, 2015). Cloud products include stereo camera photogrammetric cloud boundary locations (e.g., Figure 5; Oktem et al. 2014), GOES-16 deep convective overshooting top retrievals (Bedka and Khlopenkov 2016), and Cartesian gridded radar PPI volumes. Higher level radar products available include those generated by the Taranis radar processing framework including scanning precipitation radar corrections, specific differential phase retrievals, and geophysical retrievals. Geophysical retrievals include hydrometeor identification, rain rate, rain water content, and mass-weighted mean diameter.

- These radar products are being used to develop convective cell track and cloud type databases.
- All datasets will be made publicly available once published.

6. Preliminary Highlights and Research Opportunities

a. Meteorology

Relatively strong upper level jet westerly flow with variable meridional winds associated with passages of synoptic troughs and ridges was present for most of the campaign even during the summer. Upper level synoptic troughs crossing the Andes induced the Northwestern Argentinean Low in the lee of the Andes northwest of the SDC, which would induce northerly low-level flow over the SDC, commonly in the form of a low-level jet. This low-level northerly flow brought moisture from the Amazon into the region while the westerly flow crossing the Andes induced steep free tropospheric lapse rates and a variable height inversion layer that allowed low levels to build conditional instability.

SDC topography also modified low level flow and nearly always had an easterly upslope component, even at night when one might expect surface cooling-induced downslope westerly flow (Figure 6a). The depth of this easterly flow varied considerably such that the flow at the crest of the SDC at times switched from westerly to easterly and could be above or below inversion layers depending on the situation, as indicated by the location of sharp specific humidity drops in Figure 6c. Boundary layer northeasterly flow, at times in the form of a low-level jet, was commonly associated with increases in precipitable water (Figure 6b black line), specific humidity (Figure 6c color fill), and most unstable convective available potential energy (MUCAPE) (Figure 6c black line). Following these events, low level flow often switched to southeasterly, commonly behind MCSs or cold fronts, where stable, moist, and relatively low CCN concentrations supported warm rain formation or drizzling fog. Above this stable layer,

northerly flow commonly continued to advect in warm, moist air, sometimes for a day or more, feeding elevated deep convection decoupled from the surface.

These multi-scale circulations supported the presence of CAPE exceeding 100 J kg⁻¹ in over 50% of the 935 AMF1 radiosondes launched. Values were often modest but reached extreme values over 6000 J kg⁻¹ with levels of neutral buoyancy (LNB, i.e., parcel equilibrium level) exceeding 16 km in January (Figure 7; see further analyses in Schumacher et al. 2021). MUCAPE and LNB most often peaked in the early evening although most unstable convective inhibition (MUCIN) typically reached a minimum earlier in the afternoon (Figure 7). MUCAPE parcels originated near the surface about half of the time and thus were frequently elevated off of the surface (Figure 7) with 30% of soundings with CAPE > 100 J kg⁻¹ having most unstable parcels over 1 km above the surface. These conditions appear to be similar to the US Great Plains (e.g., Zhang and Klein 2010). The datasets collected during CACTI provide new opportunities for investigating multi-scale atmospheric, surface, and topographic processes that produce commonalities and differences between the moist convection setups in these two regions.

b. Aerosols

Many aerosol measurements during CACTI were the first ever collected in subtropical South America, providing opportunities to better understand processes that influence their formation, growth, diurnal cycle, and vertical variability within the context of other well observed regions of the world. Figure 8 shows PDFs of observed surface CN and CCN concentrations covering the whole field campaign, highlighting a large spread in values. CN concentrations (> 10 nm) were most commonly 1500-2500 cm⁻³ but often extended to higher values that at times exceeded 10⁴ cm⁻³. These higher concentrations are reflected in ~1%

supersaturation CCN concentrations that could reach values exceeding 3000 cm⁻³, although 0.2% CCN concentrations were almost always less than 1000 cm⁻³ and typically much less than that. This highlighted the common occurrence of significant spreads in CCN spectra. Surface CN and CCN concentrations exhibited a distinctive diurnal cycle in which they were minimized around 12 UTC (9 AM LT) and peaked in the early evening (Figure 8). Contributors to this diurnal variation include afternoon new particle formation and growth, an overnight peak in precipitation, and daytime easterly component boundary layer flows (Fig. 6a). These flows originate from agricultural areas and towns in and along the SDC foothills with the Córdoba metropolitan area of more than 1.5 million people centered 90 km to the northeast. This mean diurnal cycle is also very similar to that of convective instability shown in Figure 7.

Comprehensive aerosol size distribution and optical property measurements were also made, both at the surface and aboard the aircraft. The Aerosol Chemistry Speciation Monitor continuously measured mass concentrations of organics, sulfate, nitrate, ammonium, and chloride at the surface, while the miniSPLAT aboard the G-1 measured the size and mixing state of nearly 1.5 million interstitial and cloud droplet residual particles, including particles composed of oxygenated organics mixed with varying amounts of sulfates, organic amines, dust, and fresh and aged soot particles (e.g., Fast et al. 2019). These measurements will be used to better understand how aerosol properties such as chemical composition vary from below cloud to in, around, and above clouds over a range of meteorological and cloud conditions. Such information can also be combined with air mass trajectories to examine local and remote aerosol source regions and how their transport is impacted by complex terrain. For example, ongoing research shows that very high CCN conditions resulted from smoke transport from northeastern Argentina associated with biomass burning (Cancelada et al. 2019).

INP filter samples (DeMott et al. 2020a-b) were collected on all flights following Levin et al. (2019) and throughout the campaign at the AMF1 site following DeMott et al. (2018a).

Collected particles were re-suspended in ultrapure water to obtain immersion freezing INP concentrations as a function of temperature using CSU's ice spectrometer (DeMott et al. 2018b). Figure 9 shows all AMF1 spectra collected during the G-1 flight period (17 of 83 in total) compared to the aircraft spectra. Aircraft data agree in form and span with the surface data, although flight level air often contains fewer INPs at the same temperature. This is likely due to dilution through a well-mixed boundary layer and/or decoupling of flight level air from the surface. The non-log-linear shape of filter spectra, especially the "hump" at temperatures greater than -20°C, indicates a pervasive influence of biological INPs, including bacteria, fungi, and other biomolecules from plants and soils (Hill et al. 2016; 2018, O'Sullivan et al. 2018; Suski et al. 2018). To resolve the microbial/protein, organic, and inorganic INP fractions, INPs were also measured following heating (95°C) and H₂O₂ digestions of aliquots of suspensions (Suski et al. 2018). This INP data set is the largest collected in subtropical South America, and the data on INP compositions is the most comprehensive for any mid-latitude region. Recently completed analyses, being readied for publication, suggest INP source regions primarily from the northeast to southeast of the SDC, with likely important contributions from these sectors' agricultural soils. Comparison with and integration of this new INP dataset with others collected around the world is underway.

420

421

422

423

424

425

426

403

404

405

406

407

408

409

410

411

412

413

414

415

416

417

418

419

c. Aerosol-Cloud-Precipitation Interactions

The vast array of co-located aerosol, cloud, precipitation, and radiation measurements during CACTI provides unique opportunities for studying aerosol-cloud-precipitation interactions. For surface coupled clouds, the continuous 6.5-month record of meteorological conditions and surface aerosol properties allows for the examination of aerosol direct and indirect effects on shallow cumulus and stratocumulus clouds as well as deeper mixed phase

convective clouds. In particular, current research is investigating how CCN concentrations affect stratocumulus rain formation building on Borque et al. (2018), and deep convective cloud microphysical and macrophysical properties building on Varble (2018). In addition, there are opportunities to explore how INPs affect primary ice nucleation in supercooled cumulus congestus clouds.

G-1 measured CN and CCN concentrations varied by 2 orders of magnitude and often fell significantly between the boundary layer and free troposphere (Fig. 10a). Many cloud measurements were located at 3.1-3.6-km altitudes in orographic cumulus clouds although a range of lower altitude clouds on either side of the SDC were also sampled in addition to deeper congestus clouds. Peak droplet concentrations, typically collected at mid-cloud altitudes, reached more than 1000 cm⁻³ but typical values were less than 400 cm⁻³ (Fig. 10b) and often lower than the sub-cloud 0.2% CCN concentration, indicating potentially lower updraft supersaturations and/or effects of dry air entrainment. The greatest liquid water contents (LWCs) exceeding 2 g m⁻³ were observed in deep cumulus congestus clouds on November 21. Most LWCs were much lower in magnitude, although cumulus LWCs occasionally exceeded 1 g m⁻³ (Fig. 10c). Ongoing research is examining linkages between these aerosol and cloud measurements. G-1 measurements can also be used to examine cloud processing of aerosols and vertical transport from lower altitude, higher aerosol loading layers to the relatively cleaner free troposphere.

Surface measurements show many days with new particle formation and growth of aerosols while heavy rainfall events resulted in significant wet deposition. A 1-week example is shown in Figure 11 via SMPS aerosol size distribution measurements in time. Heavy rainfall on November 12 resulted in deposition of nearly all CCN up to the peak 1% supersaturations being measured and a drop in CN > 10 nm concentrations to ~100 cm⁻³. In contrast, November 14-16 rain-free days with ample solar insolation show growth of particles during the daytime from

the Aitken to accumulation (CCN) mode. Opportunities exist to further study these new particle formation, growth, and wet scavenging processes.

d. Clouds and Precipitation

Clouds and precipitation were frequent over the AMF1 site with 191 of 212 days between 1 October and 30 April producing shallow liquid clouds, 165 of which had stratiform liquid clouds of greater than 30 minutes in duration over the site. 83 days also produced deep convection over the site with 93 days producing gauge-measurable precipitation and 135 days producing disdrometer-measurable precipitation. Time-height object identification from vertically-pointing radar and lidar data constituting the ARSCL (Active Remote Sensing of Cloud Locations) product (Clothiaux et al. 2001) show more than 3,400 shallow, liquid clouds were observed, with more than 650 lasting longer than 30 minutes. It also indicates over 2,700 primarily convective clouds with cloud bases > 0°C and tops < 0°C were observed with over 540 having cloud tops < -30°C (i.e., deep convective objects). Connecting these convective elements to one another via anvils yields over 1,100 separate convective systems, ~160 of which are deep convective systems (cloud tops < -30°C).

Low level cloud cover increased significantly between the morning and late afternoon in association with orographic upslope flow (Figure 12). Rainfall also exhibited a relative maximum in the late afternoon, however overnight hours produced the greatest amount of rainfall and most frequent deep clouds (Figure 12). This is consistent with the bimodal diurnal timing of deep convection initiation shown by Cancelada et al. (2020) and similar to parts of the US Great Plains (Higgins et al. 1997; Wilson and Roberts 2006; Zhang and Klein 2010). Rainfall was spread throughout the campaign, accumulating to just over 1000 mm (Figure 12). November, January, and March all produced 200 mm or more of rainfall with November (240).

mm) having the most rainfall. December (60 mm) and February (just over 70 mm) were very suppressed in comparison. Much of this precipitation originated in heavy rainfall events frequently exceeding 50 mm with peak 1-minute rain rates exceeding 100 mm h⁻¹, the greatest of which occurred on 11-12 November 2018 with just over 100 mm of rainfall (Figure 11). Heavy rainfall events significantly increased soil moisture (Figure 12), with potential impacts on surface fluxes and boundary layer evolution for the days that followed that require investigation.

e. Shallow Convection

North-south oriented orographic cumulus cloud lines aligned with the crest of the SDC formed on most days by afternoon hours. These cloud lines most frequently developed just east of the SDC crest but occasionally formed directly over the crest or along the western foothills depending on thermodynamic and kinematic profile of the lowest few kilometers of the troposphere. On days with strong inversions, several sampled by the G-1, these cumulus lines remained shallow but would commonly expand eastward into a stratocumulus layer by early evening. These widespread cloud layers were often detectable by the Ka-band radars and at times would begin drizzling, the causes of which are currently being investigated. An example is shown in Figure 13, although liquid cloud drizzle onset cases vary significantly in their combinations of environmental and cloud properties.

Purely liquid raining clouds and drizzling fog (e.g., present as the early morning diurnal peak in Fig. 12) were also common on days with deeper precipitating clouds. These situations were often associated with stable, moist, and relatively clean low-level easterly upslope flow commonly produced by significant rainfall events. Precipitating convective clouds of moderate depth that likely contained ice were common, as were supercooled congestus clouds without

ice reaching temperatures of -20°C or colder. The processes contributing to precipitation and ice formation in these clouds as they deepen and widen are a focus for future investigation. Several G-1 flights occurred during such events to examine near and in cloud conditions with one focus on the effects of detraining near stationary, orographic cloud lines on nearby free tropospheric temperature and humidity that may reduce entrainment-driven buoyancy dilution in subsequent clouds following hypotheses summarized in Moser and Lasher-Trapp (2018).

506

507

508

509

510

511

512

513

514

515

516

517

518

519

520

521

522

523

500

501

502

503

504

505

f. Deep Convection

Some orographic congestus initiated ice and precipitation with moderate to strong radar reflectivity values over periods of 30 minutes to several hours constituting successful deep convection initiation. Cells frequently initiated in multiple locations and interacted as time progressed. To track the evolution of cells including interactions through merging and splitting with neighboring cells, cells were identified using 15-minute C-SAPR2 composite reflectivity and tracked using an updated version of FLEXTRKR (Feng et al. 2018, 2019). The mountainous terrain to the west of the site blocked PPI elevation angles up to 2-5° depending on azimuth such that shallow cells west of the SDC are not detected; however, the deep mode is well captured by using composite rather than low level reflectivity. For the ~3.5 months (October 1 - December 26, January 21 - February 5, February 22 - March 2) that the C-SAPR2 collected PPI volumes, 6895 cells were tracked with associated radar retrieved properties. An example of identified cells and their tracks is shown in Figure 14a with accumulated cell starting locations shown by density in Figure 14b, highlighting the propensity for cells to form slightly east of the highest terrain and just west of the AMF1 site. Mean cell area increases moving eastward from the high terrain, indicative of upscale growth events immediately east of the high terrain (Figure 14c). Current work involves matching radar HSRHI scans, AMF1observed atmospheric conditions, and cell tracks to form a database for the study of factors influencing deep convective cloud life cycles.

Using the cell track database and satellite-based MCS tracking, current research is focused on deep convection initiation and upscale growth processes. One focus is building on Nelson et al. (2021) to study how mesoscale and cloud-scale circulations couple with thermodynamic variability below and above cloud base to impact convective updraft properties critical to the formation of sustained precipitation. A second focus is understanding how cells evolve following sustained precipitation formation, particularly through convective downdrafts and cold pools that initiate new updrafts and may or may not promote upscale growth into MCSs. While many deep convective cells observed during CACTI grew upscale into supercells (e.g., Trapp et al. 2020) or mesoscale complexes, events during the IOP are of particular interest because of more extensive characterization via RELAMPAGO measurements. Extreme deep convective events are also a focus of investigation (e.g., Borque et al. 2020) including the 25 January 2019 event shown in Figure 15 that produced a radar echo top near 21 km above sea level in a HSRHI scan with 40-dBZ echoes extending above 19 km.

g. Modeling

A number of modeling activities focused on CACTI cases are ongoing. A regional 3-km Weather Research and Forecasting simulation covering 15 October to 30 April utilizing an aerosol-aware microphysics scheme (Thompson and Eidhammer 2014) was performed with output intended to match radar, satellite, and vertical profiling sampling frequencies to support direct model-observations comparisons (Zhang et al. 2021, submitted). Shallow orographic cloud occurrence, convection initiation, and upscale growth representation in this simulation are being evaluated including sensitivities of convective cloud life cycles to model resolution

since horizontal grid spacing > 500 m fails to fully resolve deep convective updrafts (Bryan et al. 2003, Bryan and Morrison 2012, Varble et al. 2020, Lebo and Morrison 2015, Verelle et al. 2015). Future work will also investigate sensitivities to parameterized aerosol and microphysical processes with collected aerosol datasets available for model initialization.

Large eddy simulations better resolve convective updraft thermals, and ARM is expanding their LES ARM Symbiotic Simulation and Observation (LASSO) ensemble runs originally designed for shallow cumulus cases at the ARM SGP site (Gustafson et al. 2020) to handle CACTI orographic deep convection initiation events. These nested simulations with an inner mesoscale domain grid spacing of 100 m will be run in small ensembles for up to 10 cases or more to support convective cloud processes science, coarser model assessment, and parameterization evaluation with direct linkages to field campaign measurements. Output, as well as initialization and restart files, will be freely available to the research community.

7. Summary and Lessons Learned

CACTI, together with RELAMPAGO, was the result of a large collaborative team of U.S. and Argentine scientists, facility and project managers, instrument engineers and technicians, dataset mentors, weather forecasters, and many more. Numerous challenges were encountered including delays in shipping, electrical grid dropouts, aircraft communications dropouts, and failure of C-band hardware components. The keys to overcoming these challenges were contingency planning, timely and effective communication, readiness to adjust measurement strategies, and individuals putting in extra time and effort. The success of this team resulted in a comprehensive collection of atmospheric state, aerosol, cloud, precipitation, radiation and surface measurements at the surface and aloft, providing new opportunities to study atmospheric processes critical to weather and climate in a previously data sparse region.

Several lessons can be gleaned from CACTI that may help future field campaigns be successful. First, the importance of site location cannot be overstated, so time and care should be put into site selection to best balance scientific needs with logistical limitations. This requires pre-campaign (at least 1-2 years ahead of time) research and planning with critical local support. Second, choosing appropriate sites and measurement strategies (e.g., when to launch radiosondes, how to scan a radar) also benefits greatly from pre-campaign data analysis. Third, consistent monitoring of data via near real-time quick look imagery is critical to identifying and fixing issues quickly to avoid degraded or missing data. Lastly, datasets with consistent measurement strategies (e.g., a regular radar scan sequence) are much easier to use and interpret than frequently changing strategies. However, there is also a need for innovative new techniques targeting critical phenomena (e.g., convective updrafts) that we still fail to adequately measure. Observing system simulation experiments provide a tool to formulate and test these techniques and should become standard for future major field campaigns to reduce subjectively chosen strategies.

The unique location of the experiment conducted over an entire warm season provides new opportunities for studying the life cycles of numerous convective clouds from initial cumulus formation through organization of deep convective systems within the context of thoroughly observed factors influencing their evolution. Shallow liquid clouds were observed directly overhead on 90% of the campaign days with ~160 deep convective systems and highly variable CCN and INP concentrations. Initial results show that deep convection initiation was most frequent just east of the primary SDC ridgeline west of the AMF observing site with immediate deep convective upscale growth over and east of the AMF site. The rainfall diurnal cycle has a prominent nocturnal maximum with a secondary late afternoon peak. CIN minimizes in midafternoon followed by an early evening peak in CAPE and LNB that is similar to the mean diurnal peak of CN and CCN concentrations. These findings were generally expected but

unquantified until now. Less expected were the high frequencies of elevated deep convection, drizzling fog and warm rain, aerosol growth and significant wet scavenging events, and radar echo tops reaching nearly 21 km above sea level in the SDC foothills.

The first research studies from CACTI are just being published, and much of the research targeting processes in Figure 1 is just beginning, from controls on warm rain and ice formation to determinants of updraft size, shape, strength including entrainment and detrainment, and from the formation of downdrafts and their role in cold pools and deep convective upscale growth to interactions of aerosol and cloud life cycles with one another and with complex terrain affected circulations. Such studies combined with high-resolution modeling will improve process-level understanding but also be critical for evaluating and improving aerosol and cloud process parameterizations in next-generation weather and climate models.

Acknowledgments.

We thank the U.S. DOE ARM program for funding CACTI and many other agencies and individuals for their invaluable support including ARM managers, engineers, technicians, instrument and data mentors, the ARM Data Center, and other support staff. We thank the following individuals for their significant contributions to CACTI: Kim Nitschke, Juarez Viegas, Bruno Cunha, Tercio Silva, Kaitlyn Suski, Stephen Springston, Art Sedlacek, Mike Hubbell, Dan Nelson, Mike Crocker, Pete Carroll, Matt Newburn, Albert Mendoza, Clayton Eveland, Jon Ray, Jennifer Armstrong, Andrei Lindenmaier, Pete Argay, Todd Houchins, Brad Isom, Jennifer Comstock, Hanna Goss, Conrado Javier Rodriguez, Emilia Ludueña, Julio Bourdin, Mariano Palermo, Gustavo Cabrera, and Martin Rugna. Several individuals including Eldo Avila, David Gochis, Robert Houze, Jr., Michael Jensen, Pavlos Kollias, L. Ruby Leung, Kristen Rasmussen, and Christopher Williams contributed to pre-campaign planning. We thank

RELAMPAGO PIs, graduate students, and support provided by NSF and NCAR EOL. We
greatly appreciate INVAP S.E. for providing in-country project management. We are grateful
to SMN for major in-country support, launching radiosondes and providing forecasting
support. Siting and import/export of instrumentation was critically facilitated by AMF1 site
landowner Eduardo Castro, the Villa Yacanto city council, Hamelmann Communications, the
Córdoba provincial government (Ministry of Science and Technology; Ministry of Water,
Environment and Public Services), the national government of Argentina (Ministry of Science,
Technology, and Innovation; Ministry of Foreign Affairs, International Trade, and Worship),
the US Embassy in Argentina, Fuerza Aérea Argentina, Administración Nacional de Aviación
Civil, and Aeropuertos Argentina 2000. Forecasting was additionally supported by the
University of Buenos Aires, University of Illinois, CSU and University of Washington.
Computing support was provided by the Compute and Data Environment for Science at Oak
Ridge National Laboratory, National Energy Research Scientific Computing Center at
Lawrence Berkeley National Laboratory, the University of Utah Center for High Performance
Computing, and the Computational and Information Systems Laboratory at NCAR. Funding
was provided by the U.S. DOE Office of Science Biological and Environmental Research as
part of the Atmospheric System Research program and NSF grants AGS-1661662, AGS-
1661799, and AGS-1661707. Pacific Northwest National Laboratory is operated by Battelle
for the U.S. DOE under Contract DE-AC05-76RLO1830. Lastly, we thank three anonymous
reviewers for helpful comments.

- Data Availability Statement.
- All CACTI data is available through links provided at
- 644 www.arm.gov/research/campaigns/amf2018cacti.

647	REFERENCES

- Anabor, V., D. J. Stensrud, and O. L. L. de Moraes, 2008: Serial upstream-propagating
- mesoscale convective system events over southeastern South America. Mon. Wea. Rev.,
- 650 **136**, 3087–3105, https://doi.org/10.1175/2007MWR2334.1.
- Anderson, C. J., and Coauthors, 2003: Hydrological processes in regional climate model
- simulations of the central United States flood of June-July 1993. J. Hydrometeor., 4, 584-
- 598, doi:10.1175/1525-7541(2003)004<0584:HPIRCM>2.0.CO;2.
- Bechis, H., P. Salio, and J. J. Ruiz, 2020: Drylines in Argentina: Synoptic Climatology and
- Processes Leading to Their Genesis. Mon. Wea. Rev., 148, 111–129,
- https://doi.org/10.1175/MWR-D-19-0050.1.
- Bedka, K. M., and K. Khlopenkov, 2016: A Probabilistic Multispectral Pattern Recognition
- Method for Detection of Overshooting Cloud Tops Using Passive Satellite Imager
- Observations. J. Appl. Meteor. Climatol., 55, 1983–2005, https://doi.org/10.1175/JAMC-
- 660 D-15-0249.1.
- Bharadwaj, N., J. Hardin, B. Isom, A. Lindenmaier, A. Matthews, and D. Nelson, 2018: Ka-
- Band ARM Zenith Radar Filtered Spectral Data, General Co-Polarized Mode
- 663 (KAZRSPECCMASKGECOPOL). Atmospheric Radiation Measurement (ARM) user
- facility. http://dx.doi.org/10.5439/1025218.
- Borque, P., P. Salio, M. Nicolini, and Y. G. Skabar, 2010: Environment associated with deep
- moist convection under SALLJ conditions: A case study. Wea. Forecasting, 25, 970-984,
- https://doi.org/10.1175/2010WAF2222352.1.
- Borque, P., E. P. Luke, P. Kollias, and F. Yang, 2018: Relationship between Turbulence and
- Drizzle in Continental and Marine Low Stratiform Clouds. J. Atmos. Sci., 75, 4139–4148,
- https://doi.org/10.1175/JAS-D-18-0060.1.

- Borque, P., L. Vidal, M. Rugna, T. J. Lang, M. G. Nicora, and S. W Nesbitt, 2020: Distinctive
- signals in 1-minute observations of overshooting tops and lightning activity in a severe
- supercell thunderstorm. J. Geophys. Res. Atmos., https://doi.org/10.1029/2020JD032856.
- Bryan, G. H., J. C. Wyngaard, and J. M. Fritsch, 2003: Resolution requirements for the
- simulation of deep moist convection. Mon. Wea. Rev., 131, 2394–2416,
- https://doi.org/10.1175/1520-0493(2003)131,2394:RRFTSO.2.0.CO;2.
- Bryan, G. H. and H. Morrison, 2012: Sensitivity of a simulated squall line to horizontal
- resolution and parameterization of microphysics. Mon. Wea. Rev., 140, 202-225,
- https://doi.org/10.1175/MWR-D-11-00046.1.
- Bueno Repinaldo, H. F., M. Nicolini, and Y. G. Skabar, 2015: Characterizing the Diurnal Cycle
- of Low-Level Circulation and Convergence Using CFSR Data in Southeastern South
- 682 America. J. Appl. Meteor. Climatol., **54**, 671–690, https://doi.org/10.1175/JAMC-D-14-
- 683 0114.1.
- 684 Camponogara, G., M. A. F. Silva Dias, and G. G. Carrio, 2014: Relationship between Amazon
- biomass burning aerosols and rainfall over the La Plata Basin. Atmos. Chem. Phys., 14,
- 4397-4407, https://doi.org/10.5194/acp-14-4397-2014.
- 687 Cancelada, M., P. Salio, and S. W. Nesbitt, 2019: CCN Source Regions During
- RELAMPAGO-CACTI Field Campaign. Poster, 2019 American Geophysical Union Fall
- 689 *Meeting*. https://doi.org/10.1002/essoar.10506532.1.
- 690 Cancelada, M., P. Salio, D. Vila, S.W. Nesbitt, and L. Vidal, 2020: Backward Adaptive
- Brightness Temperature Threshold Technique (BAB3T): A Methodology to Determine
- Extreme Convective Initiation Regions Using Satellite Infrared Imagery. *Remote Sens.*, 12,
- 693 337, https://doi.org/10.3390/rs12020337.

- 694 Carril, A. F., and coauthors, 2012: Performance of a multi-RCM ensemble for South Eastern
- South America, Climate Dynamics, 39, 2747-2768, https://doi.org/10.1007/s00382-012-
- 696 1573-z.
- 697 Cecil, D. J., and C. B. Blankenship, 2012: Toward a Global Climatology of Severe Hailstorms
- as Estimated by Satellite Passive Microwave Imagers. J. Climate, 25, 687-703,
- 699 https://doi.org/10.1175/JCLI-D-11-00130.1.
- 700 Cecil, D. J., D. E. Buechler, and R. J. Blakeslee, 2015: TRMM LIS Climatology of
- 701 Thunderstorm Occurrence and Conditional Lightning Flash Rates. J. Climate 28, 6536-
- 702 6547, https://doi.org/10.1175/JCLI-D-15-0124.1.
- 703 Clothiaux, E. E., and Coauthors, 2001: The ARM millimeter wave cloud radars (MMCRs) and
- the active remote sensing of clouds (ARSCL) value added product (VAP). DOE Tech.
- 705 Memo. ARM VAP-002.1.
- Dai, A., 2006: Precipitation Characteristics in Eighteen Coupled Climate Models. J. Climate,
- 707 **19**, 4605–4630, https://doi.org/10.1175/JCLI3884.1.
- Damiani, R., J. Zehnder, B. Geerts, J. Demko, S. Haimov, J. Petti, G. S. Poulos, A. Razdan, J.
- Hu, M. Leuthold, and J. French, 2008: The Cumulus, Photogrammetric, In situ, and
- Doppler Observations experiment of 2006. Bull. Amer. Meteorol. Soc., 89, 57-73,
- 711 https://doi.org/10.1175/BAMS-89-1-57.
- 712 Del Genio, A. D., J. Wu, and Y. Chen, 2012: Characteristics of mesoscale organization in WRF
- simulations of convection during TWP-ICE. J. Climate, 25, 5666-5688,
- 714 https://doi.org/10.1175/JCLI-D-11-00422.1.
- 715 Della Ceca, L. S., M. F. G. Ferreyra, A. Lyapustin, A. Chudnovsky, L. Otero, H. Carreras
- and F. Barnaba, 2018: Satellite- based view of the aerosol spatial and temporal variability

- in the Córdoba region (Argentina) using over ten years of high- resolution data. *ISPRS J.*
- 718 *Photogram. Remote Sens.*, **145**, 250–267, https://doi.org/10.1016/j.isprsjprs.2018.08.016.
- 719 DeMott, P. J., Hill, T. C. J., and McFarquhar, G., 2018a: Measurements of Aerosols, Radiation,
- and Clouds over the Southern Ocean (MARCUS) Ice Nucleating Particle Measurements
- Field Campaign Report. Ed. by Robert Stafford, ARM user facility. DOE/SC-ARM-18-
- 722 031.
- DeMott, P. J., and Coauthors, 2018b: The Fifth International Workshop on Ice Nucleation
- phase 2 (FIN-02): laboratory intercomparison of ice nucleation measurements, Atmos.
- 725 Meas. Tech., **11**, 6231-6257, https://doi.org/10.5194/amt-11-6231-2018.
- DeMott, P. J., and T. C. J. Hill, 2020: CACTI ARM Mobile Facility (AMF) Measurements of
- Ice Nucleating Particles Final Campaign Report, Ed. by Robert Stafford, ARM user facility.
- 728 DOE/SC-ARM-20-006.
- DeMott, P. J. and T. C. J. Hill, 2020: CACTI AAF Measurements of Ice Nucleating Particles
- Final Campaign Report, Ed. by Robert Stafford, ARM user facility. DOE/SC-ARM-20-
- 731 008.
- Durkee, J. D., and T. L. Mote, 2009: A climatology of warm-season mesoscale convective
- complexes in subtropical South America. *Int. J. Climatol.*, **30**, 418–431,
- 734 https://doi.org/10.1002/joc.1893.
- Durkee, J. D., T. L. Mote, and J. M. Shepherd, 2009: The contribution of mesoscale convective
- complexes to rainfall across subtropical South America. J. Climate, 22, 4590-4605,
- 737 https://doi.org/10.1175/2009JCLI2858.1.
- Fairless, T., S. Giangrande, K. Johnson, E. Clothiaux, and P. Kollias, 2018: Active Remote
- Sensing of CLouds (ARSCL) product using Ka-band ARM Zenith Radars

- 740 (ARSCLKAZR1KOLLIAS). Atmospheric Radiation Measurement (ARM) user facility.
- 741 http://dx.doi.org/10.5439/1350629.
- Fairless, T., and S. Giangrande, 2018: Interpolated Sonde (INTERPOLATEDSONDE).
- 743 Atmospheric Radiation Measurement (ARM) user facility,
- 744 http://dx.doi.org/10.5439/1095316.
- Fan, J., and Coauthors, 2017: Cloud- resolving model intercomparison of an MC3E squall line
- case: Part I Convective updrafts. J. Geophys. Res. Atmos., 122, 9351-9378,
- 747 doi:10.1002/2017JD026622.
- 748 Fast, J. D., and Coauthors, 2019: Overview of the HI-SCALE Field Campaign: A New
- Perspective on Shallow Convective Clouds. Bull. Amer. Meteor. Soc., 100, 821-840,
- 750 https://doi.org/10.1175/BAMS-D-18-0030.1.
- Feng, Z., and Coauthors, 2018: Structure and Evolution of Mesoscale Convective Systems:
- Sensitivity to Cloud Microphysics in Convection-Permitting Simulations Over the United
- 753 States. J. Adv. Model Earth Sys., **10**, 1470-1494, https://doi.org/10.1029/2018MS001305.
- Feng, Z., and Coauthors, 2019: Spatiotemporal Characteristics and Large-scale Environments
- of Mesoscale Convective Systems East of the Rocky Mountains. *J. Climate*, **32**, 7303-7328,
- 756 https://doi.org/10.1175/JCLI-D-19-0137.1.
- 757 Freitas, S. R., K. M. Longo, M. A. F. Silva Dias, P. L. S. Dias, R. Chatfield, E. Prins, P. Artaxo,
- G. A. Grell, and F. S. Recuero, 2005: Monitoring the transport of biomass-burning
- 759 emissions in South America, Environ. Fluid Mech., 5, 135–167,
- 760 https://doi.org/10.1007/s10652- 005- 0243- 7.
- 761 Fridlind, A. M., and Coauthors, 2012: A comparison of TWP-ICE observational data with
- 762 cloud-resolving model results. J. Geophys. Res., 117, D05204,
- 763 https://doi.org/10.1029/2011JD016595.

- Gustafson, W. I., and Coauthors, 2020: The Large-Eddy Simulation (LES) Atmospheric
- Radiation Measurement (ARM) Symbiotic Simulation and Observation (LASSO) Activity
- for Continental Shallow Convection. Bull. Amer. Meteor. Soc., 101, E462–E479,
- 767 https://doi.org/10.1175/BAMS-D-19-0065.1.
- Hagos, S., Z. Feng, C. D. Burleyson, K.-S. S. Lim, C. N. Long, D. Wu, and G. Thompson,
- 769 2014: Evaluation of convection-permitting model simulations of cloud populations
- associated with the Madden-Julian Oscillation using data collected during the
- AMIE/DYNAMO field campaign. J. Geophys. Res. Atmos., 119, 12,052-12,068,
- 772 https://doi.org/10.1002/2014JD022143.
- Han, B., and Coauthors, 2019: Cloud- resolving model intercomparison of an MC3E squall
- line case: Part II. Stratiform precipitation properties. *Journal of Geophysical Research*:
- 775 Atmospheres, **124**, 1090-1117, https://doi.org/10.1029/2018JD029596.
- Hardin, J., A. Hunzinger, E. Schuman, A. Matthews, N. Bharadwaj, A. Varble, K. Johnson,
- and S. Giangrande, 2018: C-band Scanning ARM Precipitation Radar, CF-Radial, Quality-
- 778 Controlled Hemispheric Range-Height Indicator Scans (CSAPR2CFRHSRHIQC).
- 779 Atmospheric Radiation Measurement (ARM) user facility,
- 780 http://dx.doi.org/10.5439/1615607.
- Hardin, J., A. Hunzinger, E. Schuman, A. Matthews, N. Bharadwaj, A. Varble, K. Johnson,
- and S. Giangrande, 2018: C-band Scanning ARM Precipitation Radar, CF-Radial, Quality-
- Controlled Plan-Position Indicator Scans (CSAPR2CFRPPIQC). Atmospheric Radiation
- Measurement (ARM) user facility, http://dx.doi.org/10.5439/1615604.
- Hardin, J., A. Hunzinger, E. Schuman, A. Matthews, N. Bharadwaj, A. Varble, K. Johnson,
- and S. Giangrande, 2018: Ka-Band Scanning ARM Cloud Radar, CF-Radial, Quality-
- 787 Controlled Hemispheric Range-Height Indicator Scans (KASACRCFRHSRHIQC).

- 788 Atmospheric Radiation Measurement (ARM) user facility,
- 789 http://dx.doi.org/10.5439/1615605.
- Hardin, J. C., A. Hunzinger, E. Schuman, A. Matthews, N. Bharadwaj, A. Varble, K. Johnson,
- and S. Giangrande, 2020: CACTI Radar b1 Processing: Corrections, Calibrations, and
- Processing Report. Ed. by Robert Stafford, ARM user facility. DOE/SC-ARM-TR-044.
- Higgins, R. W., Y. Yao, E. S. Yarosh, J. E. Janowiak, and K. C. Mo, 1997: Influence of the
- Great Plains Low-Level Jet on Summertime Precipitation and Moisture Transport over the
- 795 Central United States. J. Climate, 10, 481–507, https://doi.org/10.1175/1520-
- 796 0442(1997)010<0481:IOTGPL>2.0.CO;2.
- 797 Hill, T. C. J., P. J. DeMott, F. Conen and O. Möhler, 2018: Impacts of bioaerosols on
- atmospheric ice nucleation processes, Chapter 3.1 in *Microbiology of Aerosols*, Delort, A.-
- 799 M., and Amato, P., Eds. John Wiley & Sons, Inc., 1st Edition, ISBN 97781119132288.
- Hill, T. C. J., P. J. DeMott, Y. Tobo, J. Fröhlich-Nowoisky, B. F. Moffett, G. D. Franc, and S.
- M. Kreidenweis, 2016: Sources of organic ice nucleating particles in soils, *Atmos. Chem.*
- 802 *Phys.*, **16**, 7195–7211, https://doi.org/10.5194/acp-2016-1.
- Hohenegger, C. and B. Stevens, 2013: Preconditioning deep convection with cumulus
- 804 congestus. J. Atmos. Sci., **70**, 448-464, https://doi.org/10.1175/JAS-D-12-089.1.
- 805 Holdridge, D., E. Keeler, and J. Kyrouac, 2018: Balloon-Borne Sounding System
- 806 (SONDEWNPN). Atmospheric Radiation Measurement (ARM) user facility,
- 807 http://dx.doi.org/10.5439/1021460.
- Houze, R. A., 2012: Orographic effects on precipitating clouds, Rev. Geophys., 50, RG1001,
- https://doi.org/10.1029/2011RG000365.
- Hunzinger, A., Hardin, J. C., Bharadwaj, N., Varble, A., and Matthews, A., 2020: An extended
- radar relative calibration adjustment (eRCA) technique for higher-frequency radars and

- range-height indicator (RHI) scans, Atmos. Meas. Tech., 13, 3147-3166,
- 813 https://doi.org/10.5194/amt-13-3147-2020.
- Johnson, K., T. Fairless, and S. Giangrande, 2018: Ka-Band ARM Zenith Radar (KAZR) CF-
- Radial, Corrected VAP, General Mode (KAZRCFRCORGE). Atmospheric Radiation
- Measurement (ARM) user facility, http://dx.doi.org/10.5439/1642217.
- Klein, C., and C. M. Taylor, C., 2020: Dry soils can intensify mesoscale convective systems.
- Proceedings of the National Academy of Sciences, 117, 21132-21137,
- https://doi.org/10.1073/pnas.2007998117.
- Klein, S. A., X. Jiang, J. Boyle, S. Malyshev, and S. Xie, 2006: Diagnosis of the summertime
- warm and dry bias over the U.S. Southern Great Plains in the GFDL climate model using
- a weather forecasting approach, *Geophys. Res. Lett.*, **33**, doi:10.1029/2006GL027567.
- 823 Kollias, P., and Coauthors, 2014: Scanning ARM Cloud Radars. Part II: Data Quality
- 824 Control and Processing. J. Atmos. Oceanic Technol., 31, 583-598.
- 825 https://doi.org/10.1175/JTECH-D-13-00045.1.
- 826 Kuang, C., S. Salwen, M. Boyer, and A. Singh, 2018: Condensation Particle Counter
- 827 (AOSCPCF). Atmospheric Radiation Measurement (ARM) user facility,
- 828 http://dx.doi.org/10.5439/1046184.
- 829 Kuang, C., S. Salwen, M. Boyer, and A. Singh, 2018: Scanning Mobility Particle Sizer
- 830 (AOSSMPS). Atmospheric Radiation Measurement (ARM) user facility,
- http://dx.doi.org/10.5439/1095583.
- Kumjian, M. R., and Coauthors, 2020: Gargantuan Hail in Argentina. Bull. Amer. Meteor. Soc.,
- 833 **101**, E1241–E1258, https://doi.org/10.1175/BAMS-D-19-0012.1.
- Laing, A.G. and J. M. Fritsch, 1997: The global population of mesoscale convective
- complexes. *Q.J.R. Meteorol. Soc.*, **123**, 389-405, https://doi.org/10.1002/qj.49712353807.

- 836 Lang, S. E., W. Tao, X. Zeng, and Y. Li, 2011: Reducing the Biases in Simulated Radar
- Reflectivities from a Bulk Microphysics Scheme: Tropical Convective Systems. *J. Atmos.*
- 838 *Sci.*, **68**, 2306–2320, https://doi.org/10.1175/JAS-D-10-05000.1.
- Lebo, Z. J. and H. Morrison, 2015: Effects of Horizontal and Vertical Grid Spacing on Mixing
- in Simulated Squall Lines and Implications for Convective Strength and Structure. *Mon.*
- Wea. Rev., 143, 4355–4375, https://doi.org/10.1175/MWR-D-15-0154.1.
- Levin, E. J. T., P. J DeMott, K. J Suski, Y. Boose, T. C. J. Hill, C. S. McCluskey, G. P. Schill,
- K. Rocci, H. Al-Mashat, L. J. Kristensen, G. C. Cornwell, K. A. Prather, J. M. Tomlinson,
- F. Mei, J. Hubbe, M. S. Pekour, R. J. Sullivan, L. R. Leung and S. M. Kreidenweis, 2019:
- Characteristics of ice nucleating particles in and around California winter storms, *Journal*
- 846 of Geophysical Research: Atmospheres, 124, 11,530-11,551,
- 847 https://doi.org/10.1029/2019JD030831.
- Marinescu, P.J., S.C. van den Heever, S.M. Saleeby and S.M. Kreidenweis, 2016: The
- microphysical contributions to and evolution of latent heating profiles in two MC3E MCSs.
- 350 *J. Geophys. Res.*, **121**, 7913-7935, https://doi.org/10.1002/2016JD024762.
- Marquis, J. N., A. C. Varble, P. Robinson, T. C. Nelson, and K. Friedrich, 2021: Low-level
- mesoscale and cloud-scale interactions promoting deep convective initiation. *Mon. Wea.*
- 853 *Rev.*, accepted pending revisions.
- Mather, J. H., and J. W. Voyles, 2013: The Arm Climate Research Facility: A Review of
- Structure and Capabilities. Bull. Amer. Meteor. Soc., 94, 377–392,
- https://doi.org/10.1175/BAMS-D-11-00218.1.
- Matthews, A., and D. Nelson, 2018: Water Content Meter aboard aircraft (AAFWCM).
- Atmospheric Radiation Measurement (ARM) user facility.

- Mei, F., and M. Pekour, 2018: Cloud Condensation Nuclei Particle Counter aboard aircraft
- (AAFCCN2COLA). Atmospheric Radiation Measurement (ARM) user facility.
- Mei, F., and M. Pekour, 2018: Condensation Particle Counter aboard aircraft (AAFCPCFISO).
- 862 Atmospheric Radiation Measurements (ARM) user facility.
- http://dx.doi.org/10.5439/1368538.
- Mei, F., D. Zhang, and D. Nelson, 2018: Fast Cloud Droplet Probe aboard aircraft
- (AAFFCDP). Atmospheric Radiation Measurement (ARM) user facility.
- Morris, V., and B. Ermold, 2018: Ceilometer (CEIL). Atmospheric Radiation Measurement
- 867 (ARM) user facility, http://dx.doi.rog/10.5439/1181954.
- Moser, D. H., and S. Lasher-Trapp, 2018: Cloud-Spacing Effects upon Entrainment and
- Rainfall along a Convective Line. J. Appl. Meteor. Climatol., 57, 1865-1882,
- https://doi.org/10.1175/JAMC-D-17-0363.1.
- Mulholland, J. P., S. W. Nesbitt, R. J. Trapp, K. L. Rasmussen, and P. V. Salio, 2018:
- 872 Convective Storm Life Cycle and Environments near the Sierras de Córdoba, Argentina.
- 873 *Mon. Wea. Rev.*, **146**, 2541–2557, https://doi.org/10.1175/MWR-D-18-0081.1.
- Mulholland, J. P., S. W. Nesbitt, and R. J. Trapp, 2019: A Case Study of Terrain Influences on
- Upscale Convective Growth of a Supercell. Mon. Wea. Rev., 147, 4305-4324,
- https://doi.org/10.1175/MWR-D-19-0099.1.
- Mulholland, J. P., S. W. Nesbitt, R. J. Trapp, and J. M. Peters, 2020: The influence of terrain
- on the convective environment and associated convective morphology from an idealized
- modeling prospective. J. Atmos. Sci., 77, 3929-3949, https://doi.org/10.1175/JAS-D-19-
- 880 0190.1.

- Nelson T. C., J. Marquis, A. Varble, and K. Friedrich, 2021: Radiosonde Observations of
- 882 Environments Supporting Deep Moist Convection Initiation during RELAMPAGO-
- 883 CACTI. Mon. Wea. Rev., 149, 289-309, https://doi.org/10.1175/MWR-D-20-0148.1.
- Nesbitt, S. W., R. Cifelli, and S. A. Rutledge, 2006: Storm Morphology and Rainfall
- Characteristics of TRMM Precipitation Features. Mon. Wea. Rev., 134, 2702–2721,
- https://doi.org/10.1175/MWR3200.1.
- Newsom, R., and R. Krishnamurthy, 2018: Doppler Lidar (DLFPT). Atmospheric Radiation
- Measurement (ARM) user facility, http://dx.doi.org/10.5439/1025185.
- Nicolini, M., C. Saulo, J. C. Torres, and P. Salio, 2002: Strong South American low level jet
- 890 events characterization during warm season and implications for enhanced precipitation.
- 891 *Meteorologica*, **27,** 1–2. 59–69.
- Nicolini, M. and Y. G. Skabar, 2011: Diurnal cycle in convergence patterns in the boundary
- layer east of the Andes and convection. Atmos. Res., 100, 377-390,
- https://doi.org/10.1016/j.atmosres.2010.09.019.
- 895 Oktem, R., Prabhat, J. Lee, A. Thomas, P. Zuidema, and D. M. Romps, 2014:
- Stereophotogrammetry of oceanic clouds. J. Atmos. Oceanic Technol., **31**, 1482–1501,
- 897 https://doi.org/10.1175/JTECH-D-13-00224.1.
- 898 O'Sullivan, D., and Coauthors, 2018: Contributions of biogenic material to the atmospheric
- ice-nucleating particle population in North Western Europe. Sci. Rep., 8, 13821,
- 900 https://doi.org/10.1038/s41598-018-31981-7.
- 901 Qian, Y., and Coauthors, 2020: Neglecting irrigation contributes to the simulated summertime
- warm-and-dry bias in the central United States. npj Climate and Atmos. Sci., 3, 31,
- 903 https://doi.org/10.1038/s41612-020-00135-w.

- Rasmussen, K. L., and R. A. Houze, Jr., 2011: Orogenic convection in South America as seen
- 905 by the TRMM satellite. *Mon. Wea. Rev.*, **139**, 2399-2420, https://doi.org/10.1175/MWR-
- 906 D-10-05006.1.
- Rasmussen, K. L., M. D. Zuluaga, and R. A. Houze, Jr., 2014: Severe convection and lightning
- 908 in subtropical South America. Geophys. Res. Lett., 41, 7359-7366,
- 909 https://doi.org/10.1002/2014GL061767.
- Rasmussen, K. L., M. M. Chaplin, M. D. Zuluaga, and R. A. Houze, Jr., 2016: Contribution of
- extreme convective storms to rainfall in South America. J. Hydrometeor., 17, 353-367,
- 912 https://doi.org/10.1175/JHM-D-15-0067.1.
- Rasmussen, K. L., and R. A. Houze, Jr., 2016: Convective initiation near the Andes in
- 914 subtropical South America. Mon. Wea. Rev., 144, 2351-2374,
- 915 https://doi.org/10,1175/MWR-D-15-0068.1.
- 916 Ribeiro, B. Z., and L. F. Bosart, 2018: Elevated Mixed Layers and Associated Severe
- Thunderstorm Environments in South and North America. Mon. Wea. Rev., 146, 3–28,
- 918 https://doi.org/10.1175/MWR-D-17-0121.1.
- Plane Romatschke, U., and R. A. Houze, Jr., 2010: Extreme summer convection in South America.
- 920 *J. Climate*, **23**, 3761-3791, https://doi.org/10.1175/2010JCLI3465.1.
- Ruscica, R. C., A. A. Sörensson, and C. G. Menéndez, 2015: Pathways between soil moisture
- and precipitation in southeastern South America. Atmos. Sci. Let., 16, 267-272,
- 923 https://doi.org/10.1002/asl2.552.
- 924 Salio, P., M. Nicolini, and A. C. Saulo, 2002: Chaco low level jet events characterization during
- the austral summer season by ERA reanalysis. J. Geophys. Res., 107, 4816,
- 926 https://doi.org/10.1019/2001JD001315.

- Salio, P., M. Nicolini, and E. J. Zipser, 2007: Mesoscale convective systems over southeastern
- South America and their relationship with the South American low-level jet. Mon. Wea.
- 929 Rev., **135**, 1290-1309, https://doi.org/10.1175/MWR3305.1.
- 930 Saulo, A. C., M. E. Seluchi, and M. Nicolini, 2004: A Case Study of a Chaco Low-Level Jet
- 931 Event. Mon. Wea. Rev., 132, 2669-2683, https://doi.org/10.1175/MWR2815.1.
- 932 Saulo, C., J. Ruiz, and Y. G. Skabar, 2007: Synergism between the Low-Level Jet and
- Organized Convection at Its Exit Region. Mon. Wea. Rev., 135, 1310-1326,
- 934 https://doi.org/10.1175/MWR3317.1.
- 935 Saulo, C., L. Ferreira, J. Nogués-Paegle, M. Seluchi, and J. Ruiz, 2010: Land-Atmosphere
- Interactions during a Northwestern Argentina Low Event. Mon. Wea. Rev., 138, 2481-
- 937 2498, https://doi.org/10.1175/2010MWR3227.1.
- 938 Schmid, B., and Coauthors, 2014: The DOE ARM Aerial Facility. Bull. Amer. Meteor. Soc.,
- 939 **95**, 723–742, https://doi.org/10.1175/BAMS-D-13-00040.1.
- 940 Schumacher, R. S., D. A. Hence, S. W. Nesbitt, R. J. Trapp, K. A. Kosiba, J. Wurman, P. Salio,
- M. Rugna, A. Varble, and N. R. Kelly, 2021: Convective-storm environments in subtropical
- South America from high-frequency soundings during RELAMPAGO-CACTI. *Mon. Wea.*
- 943 *Rev.*, https://doi.org/10.1175/MWR-D-20-0293.1.
- 944 Seluchi, M. E., A. C. Saulo, M. Nicolini, and P. Satyamurty, 2003: The Northwestern
- Argentinean Low: A Study of Two Typical Events. Mon. Wea. Rev., 131, 2361-2378,
- 946 https://doi.org/10.1175/1520-0493(2003)131<2361:TNALAS>2.0.CO;2.
- 947 Seluchi, M. E., R. Garreaud, F. A. Norte, and A. C. Saulo, 2006: Influence of the Subtropical
- Andes on Baroclinic Disturbances: A Cold Front Case Study. *Mon. Wea. Rev.*, **134**, 3317-
- 949 3335, https://doi.org/10.1175/MWR3247.1.

- 950 Smith, R. B., J. R. Minder, A. D. Nugent, T. Storelvmo, D. J. Kirshbaum, R. Warren, N. Lareau,
- P. Palany, A. James, and J. Fench, 2012: Orographic precipitation in the tropics: The
- Dominica Experiment. Bull. Amer. Meteorol. Soc., 93, 1567-1579,
- 953 https://doi.org/10.1175/BAMS-D-11-00194.1.
- 954 Solman, S. A., and Coauthors, 2013: Evaluation of an ensemble regional climate model
- simulations over South America driven by the ERA-Interim reanalyses: model performance
- and uncertainties, *Climate Dynamics*, **41**, 1139-1157, https://doi.org/10.1007/s00382-013-
- 957 1667-2.
- 958 Song, H., W. Lin, Y. Lin, A. B. Wolf, R. Neggers, L. J. Donner, A. D. Del Genio, and Y. Liu,
- 2013: Evaluation of precipitation simulated by seven SCMs against the ARM observations
- at the SGP site. J. Climate, 26, 5467-5492, https://doi.org/10.1175/JCLI-D-12-00263.1.
- 961 Sörensson, A. A., and C. G. Menéndez, 2011: Soil-precipitation coupling in South America.
- 962 *Tellus*, **63A**, 56-68, https://doi.org/10.1111/j.1600-0870.2010.00468.x.
- Stanford, M. W., Varble, A., Zipser, E., Strapp, J. W., Leroy, D., Schwarzenboeck, A., Potts,
- R., and Protat, A., 2017: A ubiquitous ice size bias in simulations of tropical deep
- 965 convection. Atmos. Chem. Phys., 17, 9599-9621, https://doi.org/10.5194/acp-17-9599-
- 966 2017.
- 967 Sullivan, R., D. Cook, and E. Keeler, 2018: Surface Energy Balance System (SEBS).
- 968 Atmospheric Radiation Measurement (ARM) user facility,
- 969 http://dx.doi.org/10.5439/1025274.
- 970 Suski, K. J., T. C. J. Hill, E. J. T. Levin, A. Miller, P. J. DeMott, and S. M. Kreidenweis, 2018:
- Agricultural harvesting emissions of ice-nucleating particles, *Atmos. Chem. Phys.*, 18,
- 972 13755-13771, https://doi.org/10.5194/acp-18-13755-2018.

- 973 Taylor, C.M., R. A.M. de Jeu, F. Guichard, P.P. Harris, and W.A. Dorigo, 2012: Afternoon
- 974 rain more likely over drier soils. Nature, 489, 423-426,
- 975 https://doi.org/10.1038/nature11377.
- 976 Thompson, G., and T. Eidhammer, 2014: A Study of Aerosol Impacts on Clouds and
- Precipitation Development in a Large Winter Cyclone. J. Atmos. Sci., 71, 3636–3658,
- 978 https://doi.org/10.1175/JAS-D-13-0305.1.
- 979 Trapp, R. J., and Coauthors, 2020: Multiple-Platform and Multiple-Doppler Radar
- Observations of a Supercell Thunderstorm in South America during RELAMPAGO. *Mon.*
- 981 Wea. Rev., 148, 3225–3241, https://doi.org/10.1175/MWR-D-20-0125.1.
- 982 Uin, J., C. Salwen, and G. Senum, 2018: Cloud Condensation Nuclei Particle Counter
- 983 (AOSCCN2COLAAVG). Atmospheric Radiation Measurement (ARM) user facility.
- Varble, A., A. M. Fridlind, E. J. Zipser, A. S. Ackerman, J.- P. Chaboureau, J. Fan, A. Hill, S.
- A. McFarlane, J.- P. Pinty, and B. Shipway, 2011: Evaluation of cloud- resolving model
- 986 intercomparison simulations using TWP- ICE observations: Precipitation and cloud
- 987 structure, *J. Geophys. Res.*, **116**, D12206, https://doi.org/10.1029/2010JD015180.
- Varble, A., E. J. Zipser, A. M. Fridlind, P. Zhu, A. S. Ackerman, J.-P. Chaboureau, S. Collis,
- J. Fan, A. Hill, and B. Shipway, 2014: Evaluation of cloud-resolving and limited area model
- intercomparison simulations using TWP-ICE observations: 1. Deep convective updraft
- 991 properties, J. Geophys. Res. Atmos., 119, 13,891–13,918,
- 992 https://doi.org/10.1002/2013JD021371.
- 993 Varble, A., E. J. Zipser, A. M. Fridlind, P. Zhu, A. S. Ackerman, J.-P. Chaboureau, J. Fan, A.
- Hill, B. Shipway, and C. Williams, 2014: Evaluation of cloud-resolving and limited area
- model intercomparison simulations using TWP-ICE observations: 2. Precipitation

- 996 microphysics, *J. Geophys. Res. Atmos.*, **119**, 13,919–13,945,
- 997 https://doi.org/10.1002/2013JD021372.
- 998 Varble, A., 2018: Erroneous Attribution of Deep Convective Invigoration to Aerosol
- 999 Concentration. J. Atmos. Sci., 75, 1351–1368, https://doi.org/10.1175/JAS-D-17-0217.1.
- 1000 Varble, A., and Coauthors, 2019: Cloud, Aerosol, and Complex Terrain Interactions (CACTI)
- Field Campaign Report. Ed. by Robert Stafford, ARM user facility. DOE/SC-ARM-19-
- 1002 028.
- 1003 Varble, A., H. Morrison, and E. Zipser, 2020: Effects of under-resolved convective dynamics
- on the evolution of a squall line. Mon. Wea. Rev., 148, 289-311,
- 1005 https://doi.org/10.1175/MWR-D-19-0187.1.
- 1006 Velasco, I., and J. M. Fritsch, 1987: Mesoscale convective complexes in the Americas. J.
- 1007 Geophys. Res., 92, 9591–9613, https://doi.org/10.1029/JD092iD08p09591.
- 1008 Verrelle, A., D. Ricard, and C. Lac, 2015: Sensitivity of high-resolution idealized simulations
- of thunderstorms to horizontal resolution and turbulence parametrization. *Quart. J. Roy.*
- 1010 *Meteor. Soc.*, **141**, 433–448, https://doi.org/10.1002/qj.2363.
- Wang, D., M. Bartholomew, and E. Cromwell, 2018: Weighing Bucket Precipitation Gauge
- 1012 (WBPLUVIO2). Atmospheric Radiation Measurement (ARM) user facility.
- Wilson, J. W., and R. D. Roberts, 2006: Summary of Convective Storm Initiation and Evolution
- during IHOP: Observational and Modeling Perspective. Mon. Wea. Rev., 134, 23-47,
- 1015 https://doi.org/10.1175/MWR3069.1.
- Winker, D. M., J. L. Tuckett, B. J. Getzewich, Z. Liu, M. A. Vaughan, and R. R. Rogers, 2013:
- The global 3-D distribution of tropospheric aerosols as characterized by CALIOP. *Atmos*.
- 1018 Chem. Phys., 13, 3345–3361, https://doi.org/10.5194/acp-13-3345-2013.

1019 Wulfmeyer, V., and Coauthors, 2008: The Convective and Orographically induced 1020 **89**. Precipitation Study. Bull. Meteor. Soc., 1477-1486, Amer. 1021 https://doi.org/10.1175/2008BAMS2367.1. Zelenyuk, A., D. Imre, M. Earle, R. Easter, A. Korolev, R. Leaitch, P. Liu, A. M. Macdonald, 1022 1023 M. Ovchinnikov, and W. Strapp, 2010: In Situ Characterization of Cloud Condensation 1024 Nuclei, Interstitial, and Background Particles Using the Single Particle Mass Spectrometer, 1025 SPLAT II. Anal. Chem., 82, 7943-7951, https://doi.org/10.1021/ac1013892. 1026 Zelenyuk, A., D. Imre, J. Wilson, Z. Y. Zhang, J. Wang, and K. Mueller, 2015: Airborne Single 1027 Particle Mass Spectrometers (SPLAT II & miniSPLAT) and New Software for Data 1028 Visualization and Analysis in a Geo-Spatial Context. J. Am. Soc. Mass Spectrom., 26, 257-1029 270, https://doi.org/10.1021/jasms.8b04966. 1030 Zhang, Y., and S. A. Klein, 2010: Mechanisms Affecting the Transition from Shallow to Deep 1031 Convection over Land: Inferences from Observations of the Diurnal Cycle Collected at the 1032 ARM Southern **Plains** Site. Sci.. **67**, 2943-2959, Great J. Atmos. 1033 https://doi.org/10.1175/2010JAS3366.1. 1034 Zhang, Z., A. C. Varble, Z. Feng, J. C. Hardin, and E. J. Zipser, 2021: Growth of mesoscale 1035 convective systems in observations and a seasonal convection-permitting simulation over 1036 Argentina. Mon. Wea. Rev., submitted. 1037 Zipser, E. J., D. J. Cecil, C. Liu, S. W. Nesbitt, and D. P. Yorty, 2006: Where are the most

intense thunderstorms on Earth? Bull. Amer. Meteor. Soc., 87,

https://doi.org/10.1175/BAMS-87-8-1057.

1040

1038

1039

1041

1057–1071,

TABLES

Table 1. Ground instrumentation deployed with primary measurements provided by instrumentation. Refer to Varble et al. (2019) for notes on data quality.

Ground-Based Instruments and Measurements		
Cloud and Precipitation Measurements	Instrumentation	
Cloud and Precipitation Kinematic and Microphysical Retrievals	C-band Scanning ARM Precipitation Radar, Ka/X-band Scanning ARM Cloud Radar, Ka-band ARM Zenith Radar, Radar Wind Profiler	
Heights of Cloud Bases/Tops, Sizes, and Vertical Winds	ARM Cloud Digital Cameras	
Cloud Base Height	Ceilometer, Micropulse Lidar, Doppler lidar	
Cloud Scene/Fraction	Total Sky Imager	
Raindrop Size Distribution, Fall Speeds, and Rainfall	Parsivel Laser and 2D Video Disdrometers, Tipping and Weighing Bucket Rain Gauges, Optical Rain Gauge, Present Weather Detector	
Liquid Water Path	2-Channel, High-Frequency, and Profiling Microwave Radiometers	
Atmospheric State Measurements	Instrumentation	
Precipitable Water	2-Channel, High-Frequency, and Profiling Microwave Radiometers	
Surface Pressure, Temperature, Humidity, Winds, and Visibility	Surface Meteorological Stations (4 sites)	
Vertical Profiles of Temperature, Humidity, and Winds	Radiosondes (2 sites), Radar Wind Profiler, Profiling Microwave Radiometer, Atmospheric Emitted Radiation Interferometer	
Boundary Layer Winds and Turbulence	Doppler Lidar, Sodar	
Surface Condition Measurements	Instrumentation	

Surface Heat Fluxes and Energy Balance, CO ₂ Flux, Turbulence, and Soil Temperature and Moisture	Eddy Correlation Flux Measurement System, Surface Energy Balance System
Aerosol and Trace Gas Measurements	Instrumentation
Aerosol Backscatter Profile	Micropulse Lidar, Doppler Lidar, Ceilometer
Aerosol Optical Depth	Cimel Sun Photometer, Multifilter Rotating Shadowband Radiometer
Cloud Condensation Nuclei (CCN) Concentration	Dual Column CCN counter
Condensation Nuclei (CN) Concentration	Fine and Ultrafine Condensation Particle Counters
Ice Nucleating Particle (INP) Concentration	Filters processed in Colorado State University Ice Spectrometer
Aerosol Chemical Composition	Aerosol Chemistry Speciation Monitor, Single Particle Soot Photometer
Aerosol Scattering and Growth	Ambient and Variable Humidity Nephelometers
Aerosol Absorption	Particle Soot Absorption Photometer
Aerosol Size Distribution	Ultra-High Sensitivity Aerosol Spectrometer, Scanning Mobility Particle Sizer, Aerodynamic Particle Sizer
Trace Gas Concentrations	O ₃ , CO, N ₂ O, H ₂ O Monitoring Systems
Radiation Measurements	Instrumentation
Radiative Fluxes	Broadband Direct, Diffuse, and Total Downwelling Downwelling Radiation Radiometers, Broadband Upwelling Radiation Radiometers, Ground and Sky Infrared Thermometers, AERI, Narrow Field of View 2-Channel Zenith Radiometer, Hemispheric and Zenith Shortwave Array Spectroradiometers, Multifilter Radiometer, Multifilter Rotating Shadowband Radiometer, Cimel Sun Photometer, Surface Energy Balance System, 2-Channel, High-Frequency, and Profiling Microwave Radiometers

Table 2. G-1 aircraft instrumentation during CACTI with primary measurements of each instrument. Please see Varble et al. (2019) for data quality notes.

Aircraft Instruments and Measurements	
Positioning Measurements	Instrumentation
Position/Aircraft parameters	Aircraft Integrated Meteorological Measurement System- 20, Global Positioning System (GPS) DSM 232, C- MIGITS III (Miniature Integrated GPS/INS Tactical System), VectorNav-200 GPS/INS, Video Camera P1344
Atmospheric State Measurements	Instrumentation
Pressure, Temperature, Humidity, Winds, Turbulence	Gust Probe, Rosemount 1221F2, Aircraft Integrated Meteorological Measurement System-20, Tunable Diode Laser Hygrometer, GE-1011B Chilled Mirror Hygrometer, Licor LI-840A, Rosemount 1201F1 and E102AL
Aerosol and Trace Gas Measurements	Instrumentation
Aerosol Sampling	Aerosol Isokinetic Inlet, Counterflow Virtual Impactor (CVI) Inlet
Aerosol Optical Properties	Single Particle Soot Photometer, 3-wavelength Integrating Nephelometer, 3-wavelength Particle Soot Absorption Photometer, 3-wavelength Single Channel Tricolor Absorption Photometer
Aerosol Chemical Composition	Single Particle Mass Spectrometer (miniSPLAT)
Aerosol Size Distribution	Ultra-High Sensitivity Aerosol Spectrometer, Scanning Mobility Particle Sizer, Passive Cavity Aerosol Spectrometer, Optical Particle Counter Model Cl-3100, Dual Polarized Cloud and Aerosol Spectrometer (CAS)
CN Concentration	Fine (1 on Isokinetic Inlet and 1 on CVI Inlet) and Ultrafine CPCs
CCN Concentration	Dual-column CCN counter
INP Concentration	Filter Collections for Colorado State University Ice Spectrometer

Trace Gas Concentrations	N ₂ O, CO, O ₃ , and SO ₂ Monitoring Systems
Cloud and Precipitation Measurements	Instrumentation
Hydrometeor Size Distribution	Fast Cloud Droplet Probe, 2-Dimensional Stereo Probe, High Volume Precipitation Sampler 3, Cloud and Aerosol Precipitation Spectrometer (CAPS; includes Cloud Imaging Probe, CAS, and Hotwire Sensor)
Hydrometeor Imagery	Cloud Particle Imager
Liquid Water Content	Particle Volume Monitor 100-A, Multi-Element Water Content Meter, Hotwire Sensor from CAPS

Table 3. CACTI G-1 flights including their date, time, and situation. Flight summaries can bedownloaded from the RELAMPAGO field catalog hosted by NCAR EOL.

Flight	Time (UTC)	Situation
1	13:02–17:01 Nov 4	Deepening orographic cumulus
2	13:09–17:05 Nov 6	Deep convection initiation; likely warm rain
3	12:10–16:10 Nov 10	Deepening orographic cumulus prior to deep convection initiation
4	16:48–20:00 Nov 12	Elevated deep convection, low-level stable cumulus and stratus
5	14:00–18:00 Nov 14	Clear air aerosol sampling
6	13:05–16:00 Nov 15	Clear air aerosol sampling
7	14:05–18:00 Nov 16	Boundary layer and elevated orographic cumulus
8	12:18–16:30 Nov 17	Congestus along cold front; wind-blown dust; mountain wave
9	15:10–19:06 Nov 20	Orographic cumulus; strong inversion
10	18:22–20:27 Nov 21	Orographic congestus and deep convection initiation
11	14:31–18:11 Nov 22	Stratiform anvil sampling along radar north-south scans
12	16:17–20:25 Nov 24	Orographic cumulus line; strong inversion
13	15:51–19:07 Nov 25	Orographic cumulus line; potential decoupling from boundary layer
14	15:08–18:50 Nov 28	Orographic congestus and deep convection initiation
15	14:16–16:32 Nov 29	Orographic congestus and deep convection initiation
16	16:20–18:47 Dec 1	Elevated drizzle in orographic stratocumulus; possible ice
17	12:06–16:11 Dec 2	Elevated drizzle in widespread clouds; possible ice; gravity waves in cloud layer
18	16:03–20:09 Dec 3	Boundary layer coupled orographic cumulus; strong inversion
19	17:51–19:45 Dec 4	Deepening congestus and some deep convection initiation

20	12:04–15:28 Dec 5	Mid-level clouds; congestus and some deep convection initiation
21	15:01–19:01 Dec 7	Orographic cumulus; strengthening inversion
22	16:06–19:30 Dec 8	Clear air aerosol sampling

1053 FIGURES

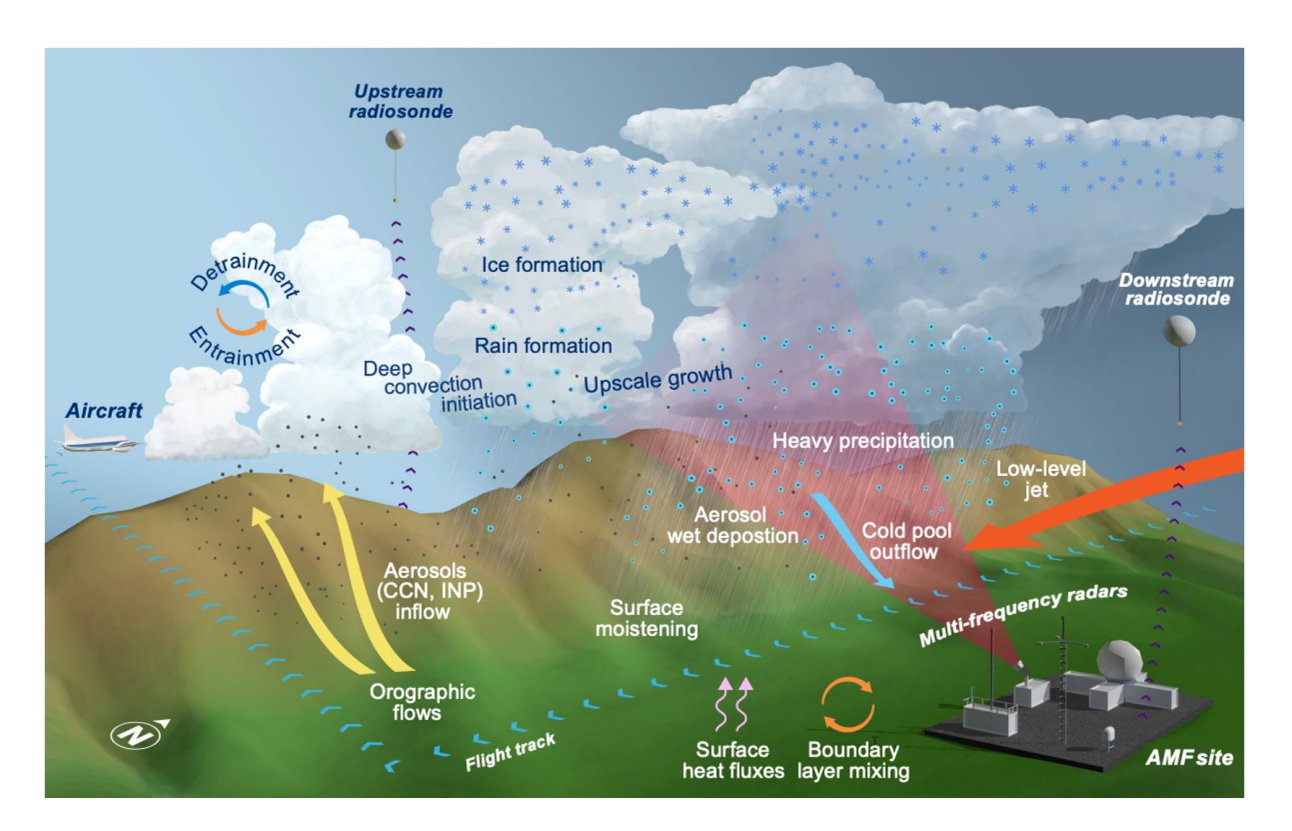


Figure 1. A conceptual rendering of the atmospheric processes targeted by CACTI with some of the critical observing platforms.

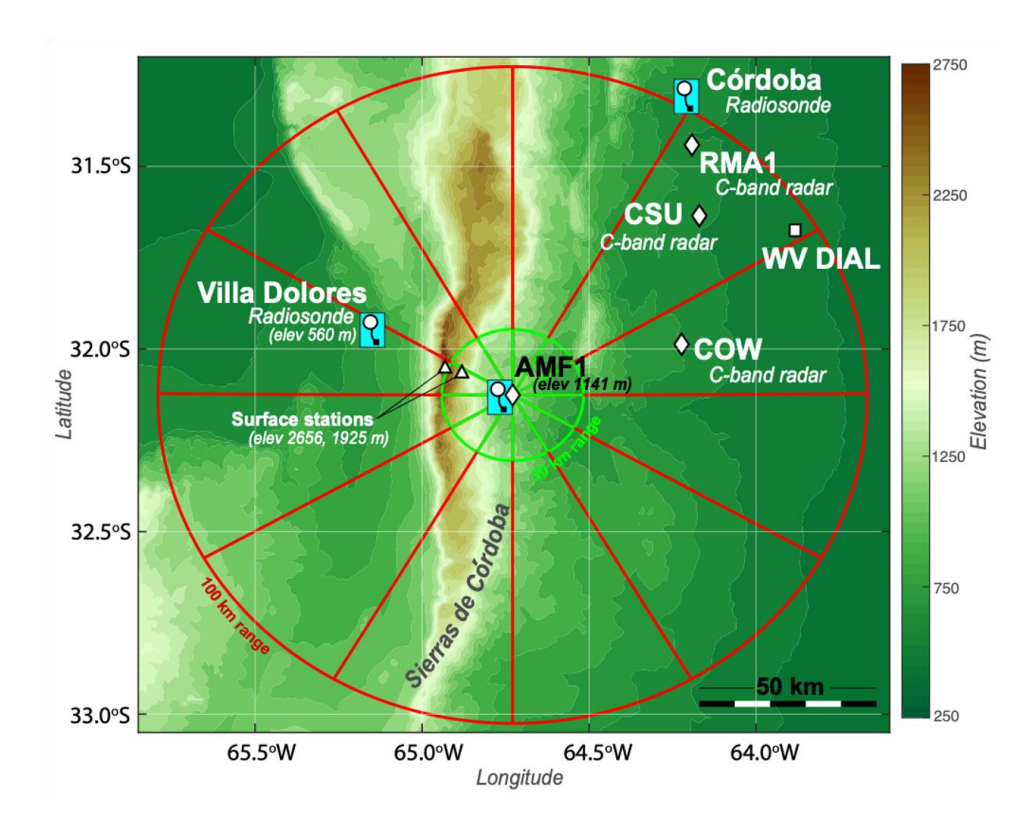


Figure 2. A map of the CACTI observing domain highlighting the Sierras de Córdoba range, the AMF1 site, high elevation meteorological stations, and the second sounding site. Hemispheric RHIs were performed by the scanning radars along the radials shown. The Argentine operational RMA1 C-band radar and Córdoba sounding sites, and fixed RELAMPAGO C-band radar and differential absorption lidar (WV DIAL) sites, are also shown.



Figure 3. (a) A view west across the AMF1 site toward the crest of the Sierras de Córdoba range. Aerial views of the AMF1 site (b) looking toward the northwest and (c) zoomed in on

the site.

1066

1070

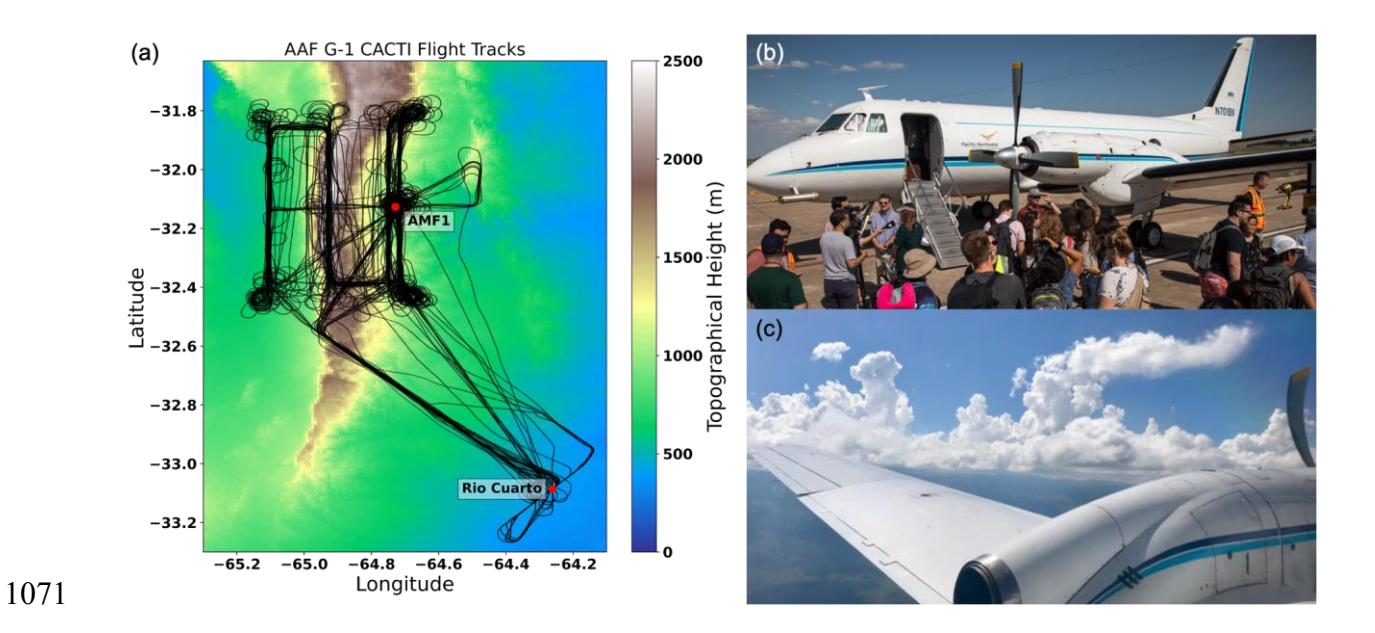


Figure 4. (a) A map overlaid with the 22 flight tracks, (b) an outreach event on 15 November 2018, and (c) cumulus congestus with ice formation from Flight 10 on 21 November 2018.



Figure 5. An example of stereo photogrammetric retrieved (a) heights of cloud boundaries, (b) manually tracked growing congestus top tracks, and (c) heights of tracked growing congestus tops in time on 19 December 2018 from 1904 to 1915 UTC.

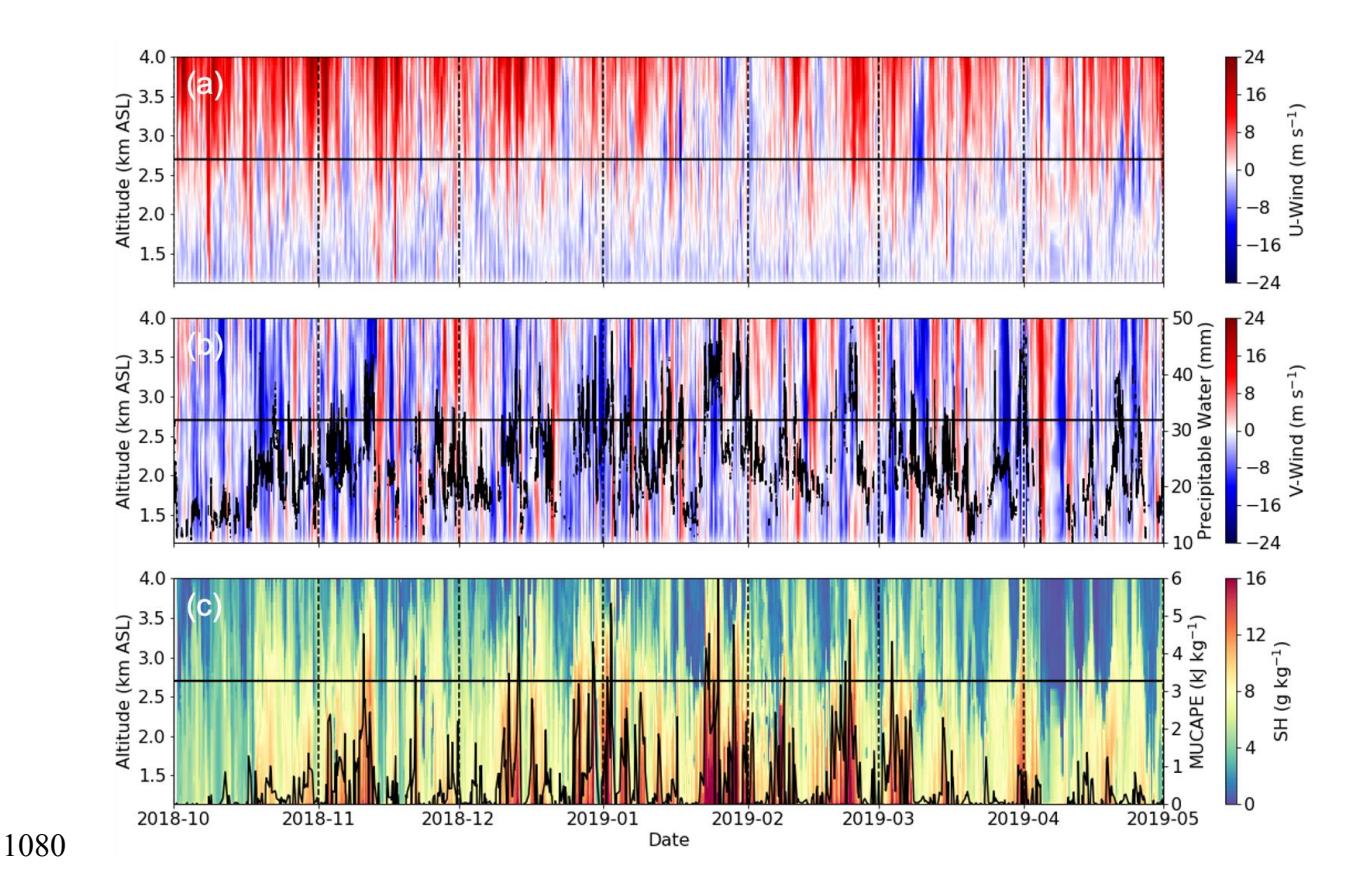


Figure 6. Low level (a) zonal wind (positive toward the east), (b) meridional wind (positive toward the north; color fill) with microwave radiometer-retrieved precipitable water (black), and (c) specific humidity (color fill) with radiosonde MUCAPE (black) for the entire campaign from the ARM INTERPOLATEDSONDE product (Fairless and Giangrande 2018). The SDC ridgeline height west of the AMF site is represented by the horizontal black line.

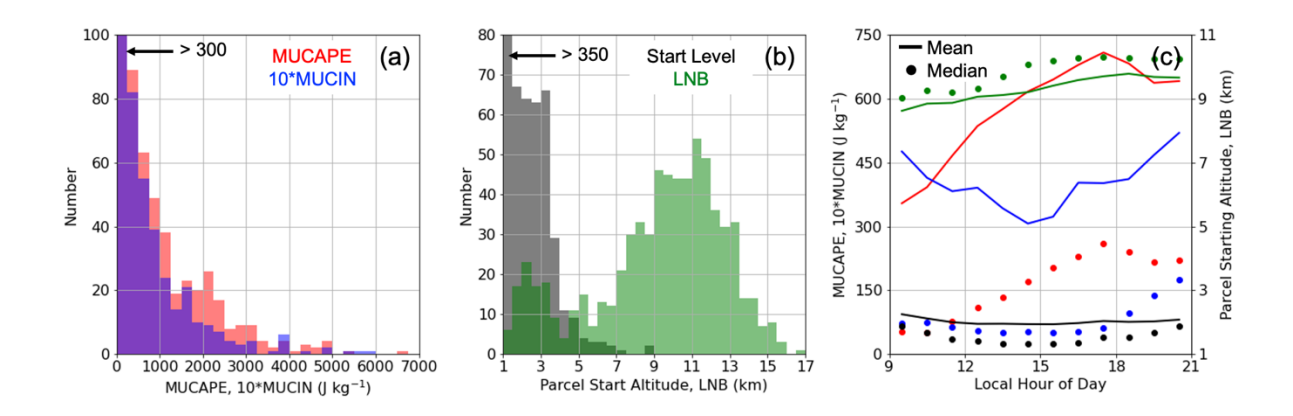


Figure 7. AMF1 radiosonde (Holdridge et al. 2018) (a) MUCAPE (red) and MUCIN (blue; multiplied by 10) PDFs, and (b) MU lifted parcel starting level (black) and LNB (green) over the entire field campaign between October 2018 and April 2019. (c) Mean and median MUCAPE (red), MUCIN (blue), MU lifted parcel starting level (black), and LNB (green) diurnal cycles between 12 and 00 UTC (9 AM - 9 PM; the daily period over which sondes were launched every 3-4 hours) from INTERPOLATEDSONDE are also shown.

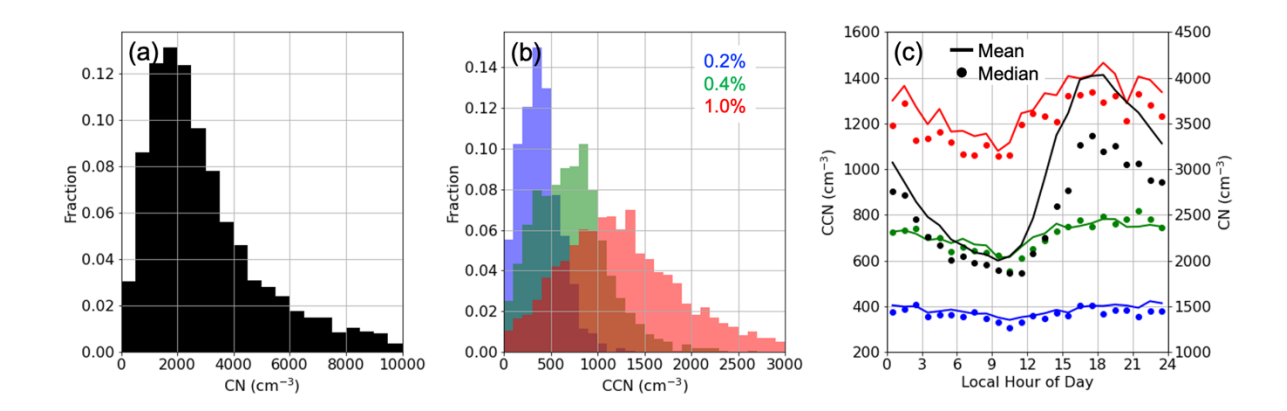


Figure 8. AMF1 site (a) CN > 10 nm (Kuang et al. 2018a) PDF and (b) CCN (Uin et al. 2018) PDFs colored by supersaturation setpoint (0.2, 0.4, and 1.0%) for the entire field campaign between October 2018 and April 2019. (c) Mean and median CN (black) and CCN (colored by supersaturation) diurnal cycles are also shown.

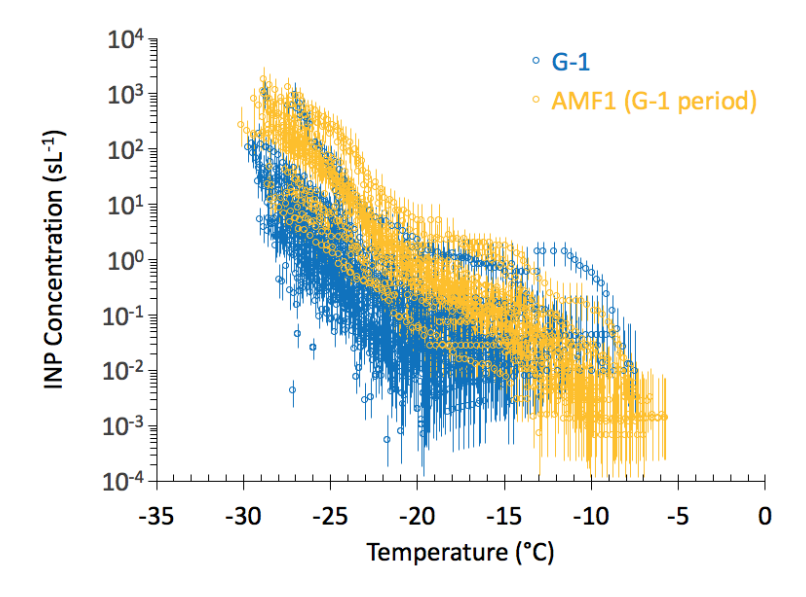


Figure 9. INP concentrations plotted versus temperature for particles from 34 filters collected on the G-1 and 17 filters collected at the AMF1 site on coincident days. Vertical bars represent 95% confidence intervals.

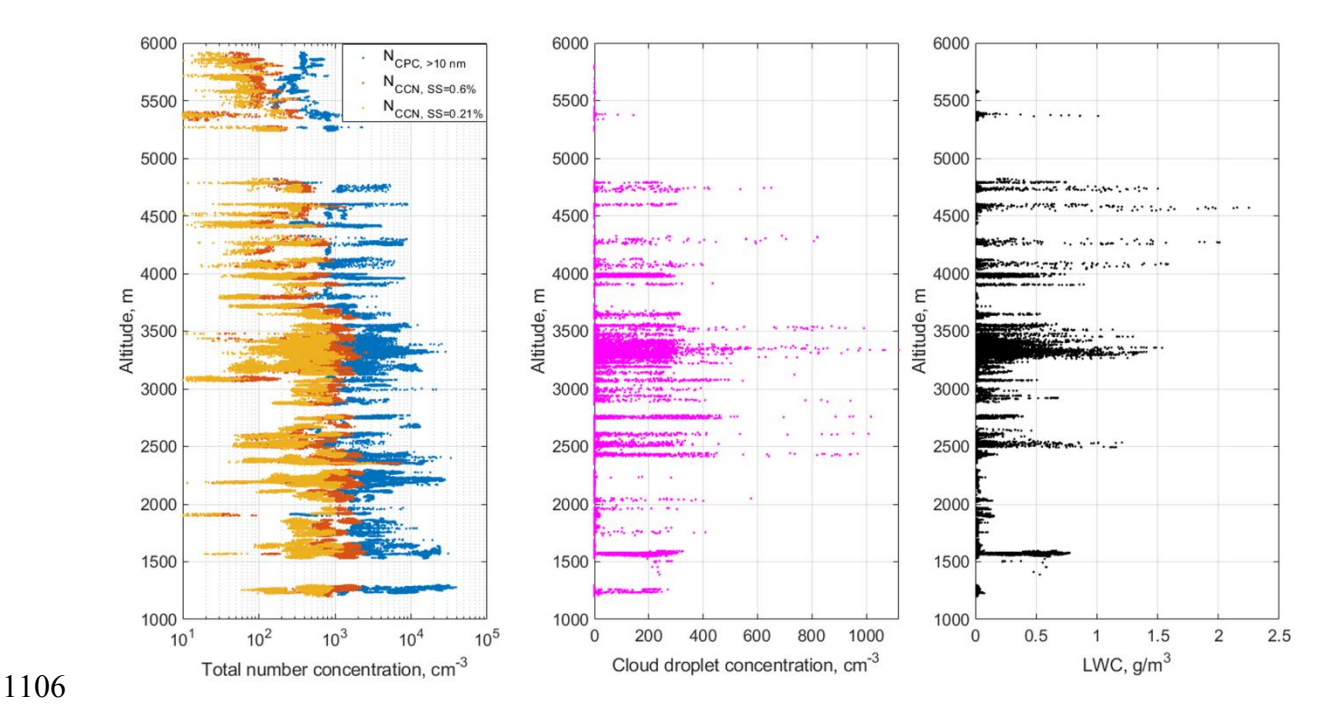


Figure 10. Cumulative 1-Hz G-1 measurements by altitude of (a) out-of-cloud CN (Mei and Pekour 2018b; blue), 0.21% CCN (Mei and Pekour 2018a; light orange), and 0.6% CCN (dark orange), (b) combined Fast Cloud Droplet Probe, 2-Dimensional Stereo Probe, and High Volume Precipitation Sampler cloud and rain droplet number concentration (Mei et al. 2018), and (c) Multi-Element Water Content Meter liquid water content (Matthews and Nelson 2018).

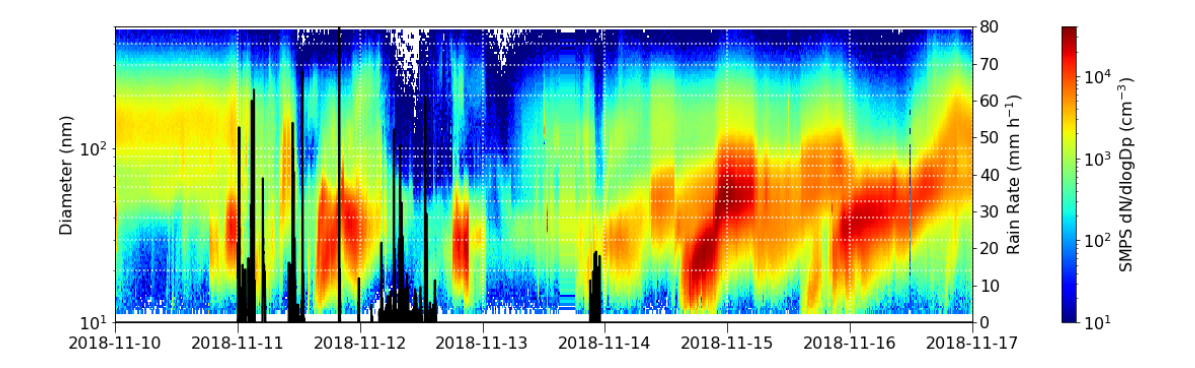


Figure 11. Surface Scanning Mobility Particle Sizer aerosol size distribution (Kuang et al. 2018b; color fill) with Pluvio-2 1-minute rain rate (Wang et al. 2018; black) between 10-16 November 2018.

1117

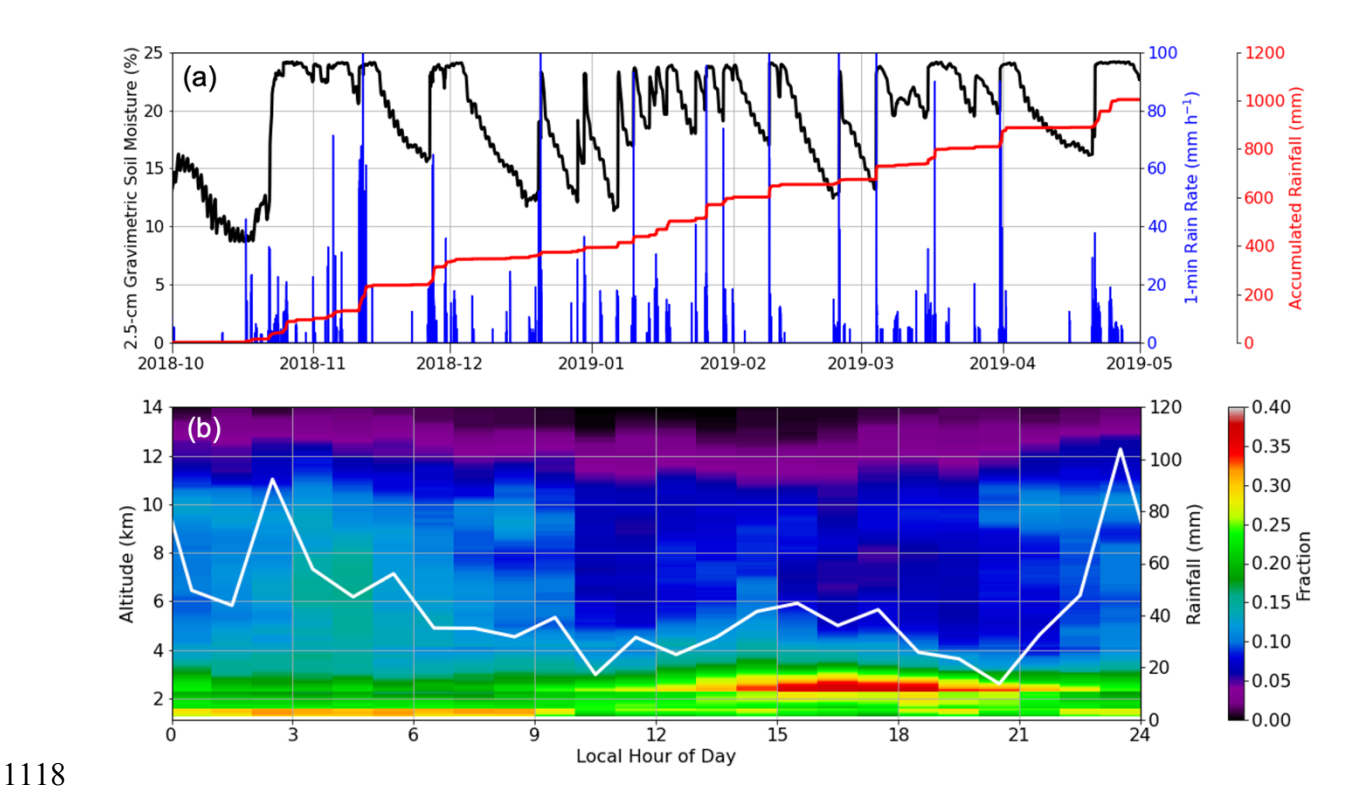


Figure 12. (a) AMF1 Pluvio-2 1-minute rain rate (blue) and accumulated rainfall (red) with soil moisture measurements (Sullivan et al. 2018) for the entire campaign. (b) Diurnal cycles of mean Ka-band ARM Zenith Radar (KAZR) measured cloud and precipitation fraction by altitude from the ARSCL product (Fairless et al. 2018; color fill) and Pluvio-2 surface accumulated precipitation (white) between October 2018 and April 2019.

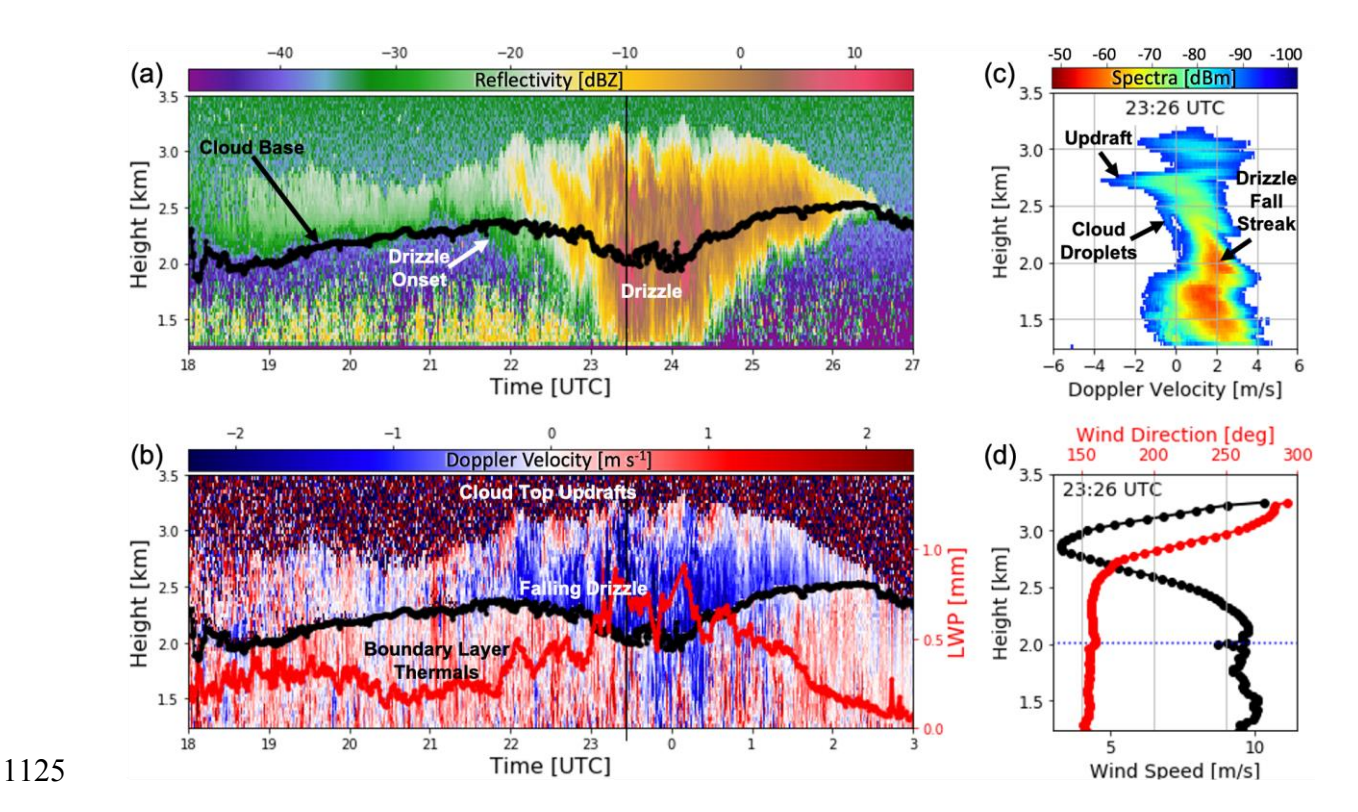


Figure 13. An example stratocumulus event with drizzle onset. Left panels show a 9-h time-height of (a) KAZR reflectivity (Johnson et al. 2018) and ceilometer (Morris and Ermold 2018) cloud base, and (b) combined KAZR and Doppler lidar (Newsom and Krishnamurthy 2018) mean Doppler velocity with microwave radiometer-retrieved liquid water path. Right panels show 2326 UTC vertical profiles of (c) KAZR Doppler spectra (Bharadwaj et al. 2018) and (d) combined Doppler lidar and Ka-band Scanning ARM Cloud Radar (Ka-SACR; Hardin et al. 2018c) velocity azimuth display horizontal wind retrievals (Kollias et al. 2014).

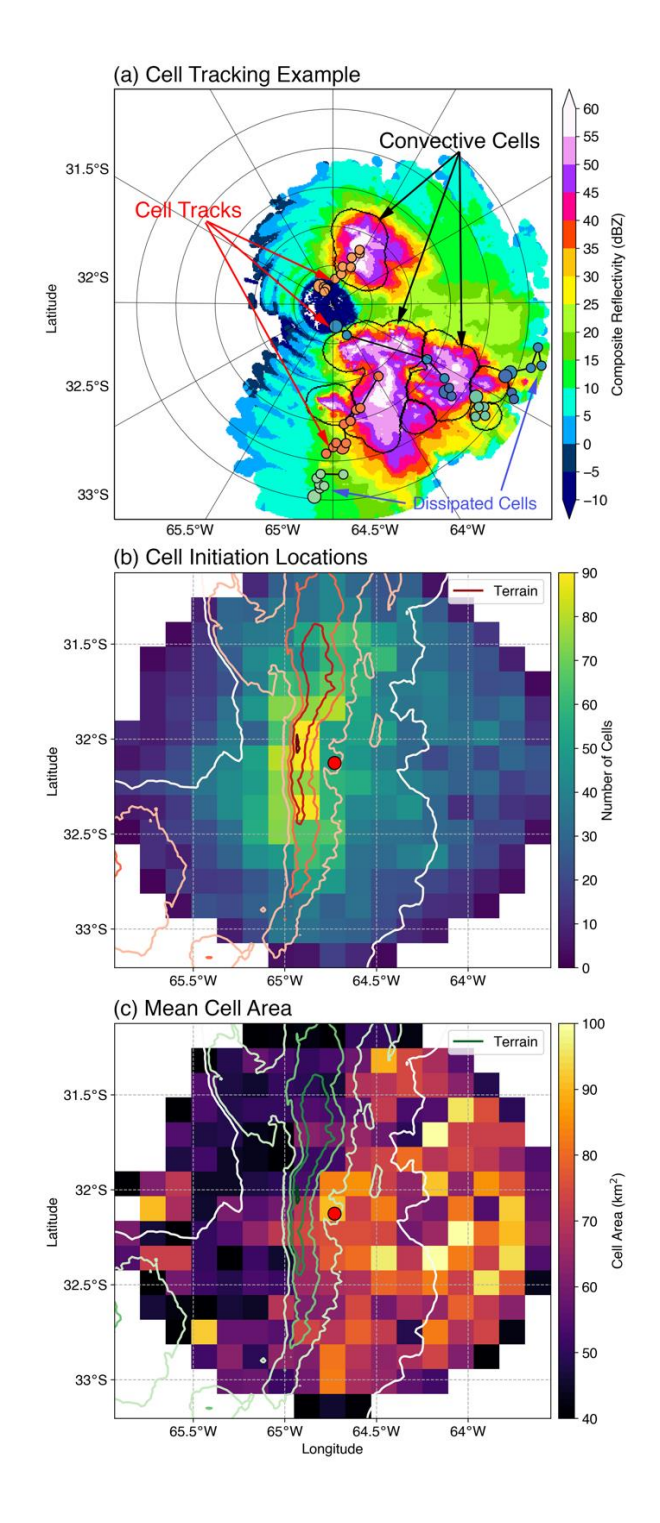


Figure 14. (a) An example of C-SAPR2 identified convective cells outlined in black on composite reflectivity with individual cell tracks shown by connected colored symbols. (b) Cell starting locations by number. (c) The mean area of cells by location where terrain height is contoured every 500 m.

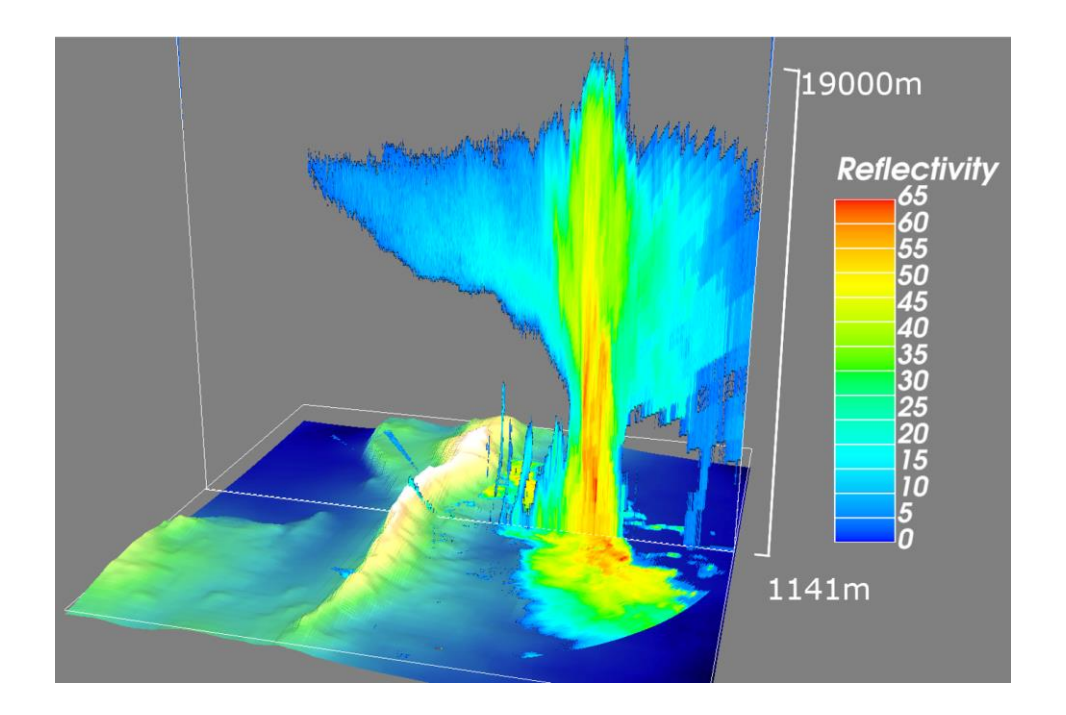


Figure 15. A three-dimensional view toward the north-northwest of the SDC terrain colored by elevation with C-SAPR2 reflectivity observed by a HSRHI scan (Hardin et al. 2018a) and low elevation PPI scan (Hardin et al. 2018b) slightly offset in time during the 25 January 2019 extreme deep convection event.